Measurement 292 (2026) 123436

Contents lists available at ScienceDirect

Measurement

journal homepage: www.elsevier.com/locate/measurement

A novel experimental platform for new types of optical measurements in the deep cryogenic regime

Kamil Leon Sołtys *, Michał Słowiński, Marcin Makowski, Bogdan Bednarski, Kamil Stankiewicz, Paweł Olejarczyk, Szymon Wójtewicz, Daniel Lisak, Mariusz Piwiński, Piotr Wcisło

Institute of Physics, Faculty of Physics, Astronomy and Informatics, Nicolaus Copernicus University in Toruń, Grudziądzka 5, 87-100 Toruń, Poland

ARTICLE INFO

Keywords:
Cryogenics
Spectroscopy

ABSTRACT

We demonstrate a novel platform for cryogenic measurements, recently launched in our laboratory, that is characterized by high stability and high uniformity of temperature, as well as a low level of mechanical noise and vibrations. It allowed us to extend, for the first time, the optical-cavity-enhanced spectroscopy technologies from room temperatures down to a deep cryogenic regime (to below 5 K). The unique feature of the system is a large high-vacuum cryogenic volume of nearly 9 l and long axial dimension of 78 cm, which makes it well suited for operating optical-cavity-based spectrometers. In order to meet the strict requirements necessary to operate optical resonators, the system is equipped with multiple stages of heavy copper blocks and flexible thermal connectors that altogether not only serve as an excellent low-pass filter for temperature fluctuations (mainly originating from cryocooler operation cycle), but also isolate the cryogenic vacuum chamber from external noise and cryocooler vibrations well enough to operate optical cavity. The system design ensures nearly perfect temperature uniformity across the main copper cylinder of the experimental cryogenic chamber that is critical for ultra-accurate spectroscopic measurements at deep cryogenic conditions. Recently, we demonstrated [Nature Physics 22, 637 (2026)] that this system opens a way to new types of measurements that were not possible before, such as an accurate test of the quantum electrodynamics for molecules, realization of the primary SI standards for temperature, concentration, and pressure in the deep cryogenic regime, measurement of the H_2 phase diagram, and determination of the ortho-para spin isomer conversion rate.

1. Introduction

Measurements performed under cryogenic conditions play a central role in modern physics, chemistry, and precision metrology, enabling access to regimes unattainable at room temperature. Recently, cryogenic conditions have become particularly important in ultra-accurate measurements in atomic, molecular, and optical (AMO) physics. Lowering the temperature leads to a substantial reduction in thermal noise, an extension of coherence times, and a narrowing of spectral features, which directly improve the accuracy, resolution, and stability of optical spectroscopic measurements. These conditions are essential for the quantitative determination of fundamental physical properties, including precision tests of quantum electrodynamics (QED) in molecules and accurate measurements of thermodynamic quantities. For these reasons, the development of experimental platforms capable of providing highly stable, homogeneous, and low-noise cryogenic environments is of fundamental importance for a wide range of high-precision measurement applications.

A variety of advanced cryogenic systems for AMO-physics measurements have been developed over the past few years to meet these demands. These include cryogenic optical cavities for ultra-stable laser frequency references and precision spectroscopy [1–9], cryogenic ion traps for spectroscopic tests of fundamental physics [10–14], as well as platforms for quantum metrology, including optical clocks based on cold atoms and ions [15,16] and quantum simulations [17]. In parallel, high-resolution molecular spectroscopy at cryogenic temperatures has been extensively developed, enabling precise studies of cold molecular systems. These include, for example, buffer-gas cooling of molecules [18–20] and investigations of weakly bound hydrogen

* Corresponding author.
E-mail addresses: kamil.leon.soltys@umk.pl (K.L. Sołtys), piotr.wcislo@umk.pl (P. Wcisło).

https://doi.org/10.1016/j.measurement.2026.123436
Received 5 May 2026; Received in revised form 17 September 2026; Accepted 5 October 2026
Available online 10 October 2026
0263-2241/© 2026 The Authors. Published by Elsevier Ltd. This is an open access article under the CC BY-NC license (http://creativecommons.org/licenses/by-nc/4.0/).

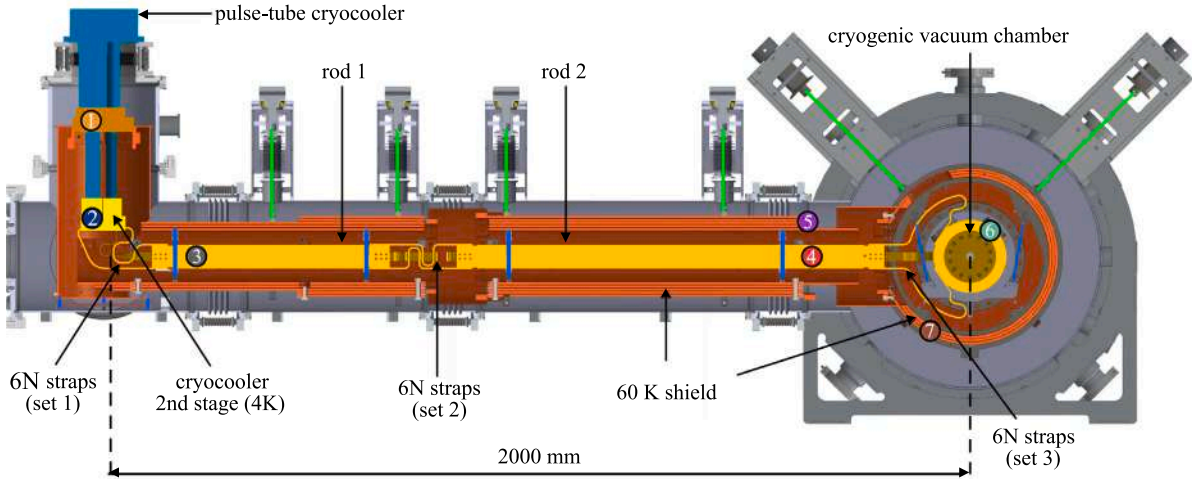

Fig. 1. Cross-section of the cryogenic system. Orange and yellow colours correspond to the first (thermal shields at $T \approx 60$ K) and second ($T \approx 4$ K) stages of the cryogenic system. The first-stage shields are suspended on stainless-steel wires (green lines), while the second-stage components are suspended on titanium wires (blue lines); the exception are titanium rods that support the vertical-cylinder thermal shields of the cryocooler (small blue lines underneath the cryocooler shields). For clarity, the first-stage thermal straps and half of the second-stage thermal straps are not shown in this figure. The numbers from 1 to 7 illustrate the positions of the temperature sensors; the numbering and colour code is consistent with Fig. 3. Sensors 1 and 2 are directly attached to the first and second stages of the cryocooler, respectively. Sensors 3 and 4 is directly attached to rods 1 and 2, respectively. Sensor 5 is directly attached to the most inner layer of the shield of rod 2. Sensor 6 is directly attached to the main copper cylinder of the cryogenic vacuum chamber. Sensor 7 is directly attach to the most outer layer of the thermal shield of the cryogenic vacuum chamber.

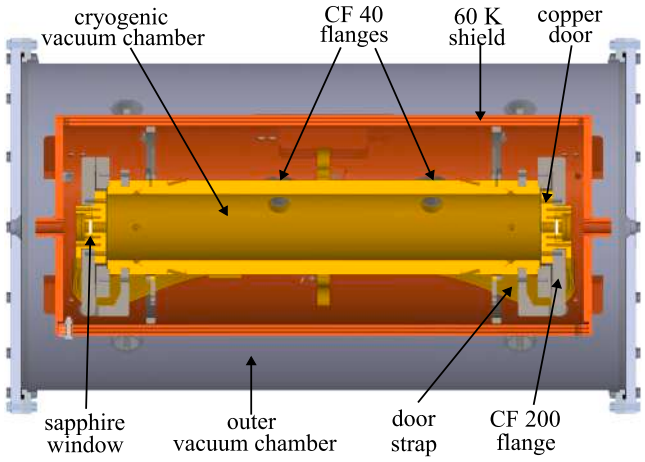

Fig. 2. Cross-section of the system along the axis of cryogenic vacuum chamber. Orange and yellow colours correspond to the first (thermal shields at $T \approx 60$ K) and second ($T \approx 4$ K) stages of the cryogenic system.

dimers and collision-induced spectra of H_2–H_2 complexes [21,22]. Such studies provide benchmark data for spectroscopic modelling relevant to atmospheric and astrophysical environments [23–25]. Other important implementations include cryogenic vacuum systems for precision sensing and quantum computing [26,27], as well as large-scale, application-oriented cryogenic infrastructures [28,29]. Across these efforts, significant attention has been devoted to engineering challenges such as thermal insulation, cryocooler integration, and mechanical stability [30–32].

Despite this substantial progress, achieving high-temperature stability, a large volume of a cryogenic measurement chamber, excellent spatial uniformity, and low mechanical vibration levels simultaneously remains a major technological challenge. In many previous works, particular emphasis has been placed on isolation and suppression of mechanical vibrations arising from cryocooler operation, which are crucial for maintaining the stability of optical resonators, trapped-ion systems, and superconducting quantum-interference devices [33–35]. In contrast, comparatively less attention has been given to a detailed, systematic analysis of thermal properties, including both steady-state temperature distributions and dynamic thermal responses [36–38]. These factors have a direct and often major impact on achievable measurement accuracy, long-term stability, and reproducibility in cryogenic spectroscopic systems.

In this article, we present a detailed technical characterization of a cryogenic vacuum chamber developed to operate an optical cavity, recently used in our laboratory to obtain the results reported in [39]. The system enables, for the first time, the extension of optical-cavity-enhanced spectroscopy techniques from room temperature to a deep-cryogenic regime (below 5 K). A distinctive feature of the setup is its large cryogenic volume of approximately 9 l combined with a long axial dimension of 78 cm, making it particularly well suited for cavity-based spectroscopic measurements. As demonstrated in Ref. [39], the system has already enabled one of the most accurate tests of quantum electrodynamics for molecules, the realization of primary SI standards for temperature, concentration, and pressure in the deep cryogenic regime, the measurement of the H_2 phase diagram, and the determination of the ortho-para spin isomer conversion rate.

In contrast to previous studies focusing primarily on mechanical isolation, the present work emphasizes a comprehensive thermal analysis of the system. We investigate both the steady-state temperature distribution and the dynamic response to thermal perturbations, demonstrating that a multi-stage structure composed of massive copper blocks and flexible thermal links acts as an efficient low-pass filter for temperature fluctuations, particularly those induced by the cryocooler cycle. This design ensures a high degree of temperature uniformity across the experimental volume while simultaneously contributing to the suppression of mechanical noise. Furthermore, we provide detailed technological insights and performance characteristics of the system, which may serve as a practical guidance for the design and implementation of advanced cryogenic platforms for high-precision measurements in a broad range of scientific and technological applications. We also provide quantitative analysis of the relevant thermal properties. One should note, however, that for such a complex system there are many unknowns (mainly related to material properties) that prevented us from providing an accurate predictive model of the thermal performance of the entire setup. Our quantitative analysis

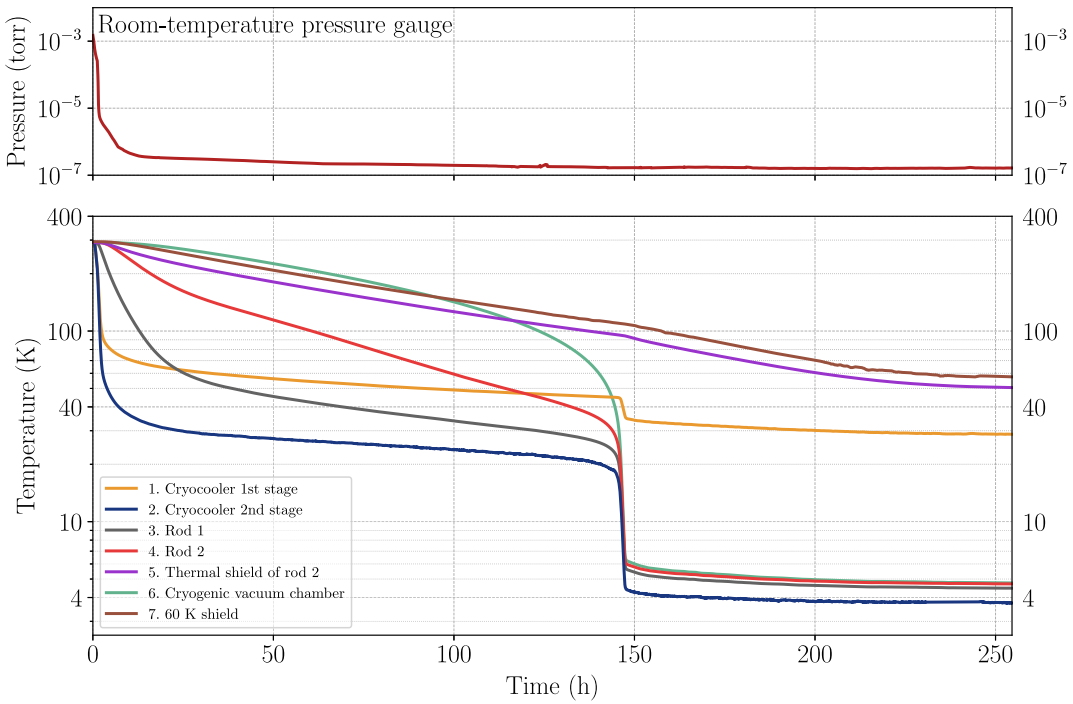

Fig. 3. Pressure (upper panel) and temperature (lower panel) during system cooling. Pressure is measured with room-temperature pressure gauge installed at the outer room-temperature vacuum chamber. The numbering (from 1 to 7) and the corresponding colour code is consistent with Fig. 1. Curves 1. and 2. (temperatures at the first and second stages of the cryocooler) were digitally filtered to remove high-frequency (0.6 Hz) temperature oscillations present at the cryocooler's head, since the goal of this figure is to illustrate the slowly varying process of system cooling. The detailed analysis of the fast temperature oscillations and the system for attenuating them are provided in Section 6.

should be treated as estimates based on the standard literature and textbook data that constitutes a practical guidance on how the standard estimations deviates from actual realization.

2. Design overview

An overview of the cryogenic setup is shown in Fig. 1. The setup consists of two independent vacuum systems. The outer, room temperature, vacuum system (the grey layers in Fig. 1) maintains the necessary conditions for the operation of the cryogenic components. The inner cryogenic vacuum chamber (whose cross-section is shown as a yellow ring on the right side of Fig. 1) is at the heart of the setup. It has a form of a long copper cylinder (with an optical access from both sides) inside which an optical instrument can be placed (recently, we used it for operating a high-finesse optical cavity for accurate molecular spectroscopy [39]). The longitudinal cross-section of the cryogenic vacuum chamber is shown in Fig. 2. The two vacuum systems are independent, which means that the inner cryogenic vacuum chamber can be filled with a gas sample for spectroscopic measurements without affecting the outer vacuum. The temperature of the cryogenic vacuum chamber can be tuned from room temperature down to 4 K. The unique features of the cryogenic vacuum chamber are its large dimensions (the inner diameter and length of the cryogenic chamber are 120 mm and 785 mm, respectively) and thickness of its walls (25 mm). Thick walls ensure exceptionally low temperature gradients across the entire chamber and large thermal and mechanical inertia, which are beneficial for damping mechanical vibrations and temperature fluctuations.

A major challenge in designing such cryogenic systems is that the principle of operation of the pulse-tube cryocoolers implies a relatively large level of temperature fluctuations at 4 K cold tip and a large level of mechanical vibrations, while precision optical metrology requires exactly opposite conditions. To overcome this problem, we place the cryogenic vacuum chamber two metres away from the cryocooler and install in between a set of two heavy copper rods (rods 1 and 2 in Fig. 1) altogether thermally linked in series with flexible high-purity copper straps, which efficiently attenuate temperature fluctuations and mechanical vibrations originating from the cryocooler.

The cryogenic vacuum chamber and copper rods (the yellow parts in Fig. 1 to which we refer as the second stage of the cryogenic system) are surrounded by 60 K copper thermal shields to reduce the thermal radiation heat load, see the orange cylindrical layers in Figs. 1 and 2 (we refer to the 60 K components as the first-stage cryogenic system). The structure of the 60 K shields is similar to the second stage, i.e., the shields of the cryogenic vacuum chamber are separated from the cryocooler by two massive copper cylindrical shields of rods 1 and 2 thermally linked in series with flexible thermal straps. Besides blocking thermal radiation, the 60 K thermal shields play also another important role, namely, they introduce a large mechanical inertia which further attenuate cryocooler and external vibrations.

3. Room-temperature outer vacuum system

The main role of the outer vacuum system (the grey layers in Fig. 1) is to establish conditions necessary for operating the cryogenic components. Besides this, it also considerably reduces convection heat loss and acoustic vibrations. All these goals do not require high vacuum level, hence it is sufficient to use the standard KF flanges that are based on Viton vacuum gaskets. The entire outer vacuum system has a volume of approximately 0.44 m^3. Before turning on the cryocooler, we evacuate the vacuum system (with all components remaining at room temperature) using a turbomolecular vacuum pump (Edwards Vacuum nEXT300, pumping speed of 300 l/s) with a dry oil-free prepump (Edwards Vacuum nXDS6i scroll pump, pumping speed of 6.2 m^3/h). These pumps allow us to achieve a vacuum level of 10^{-5} Torr, while the cryocooler can be safely turned on at 10^{-3} Torr, see Fig. 3. The large area of the surfaces of the cryogenic components (13.3 m^2 at 60 K and 1.64 m^2 at 4 K) serves as a highly efficient cryogenic pump allowing us to turn off the turbomolecular pump when the cryogenic

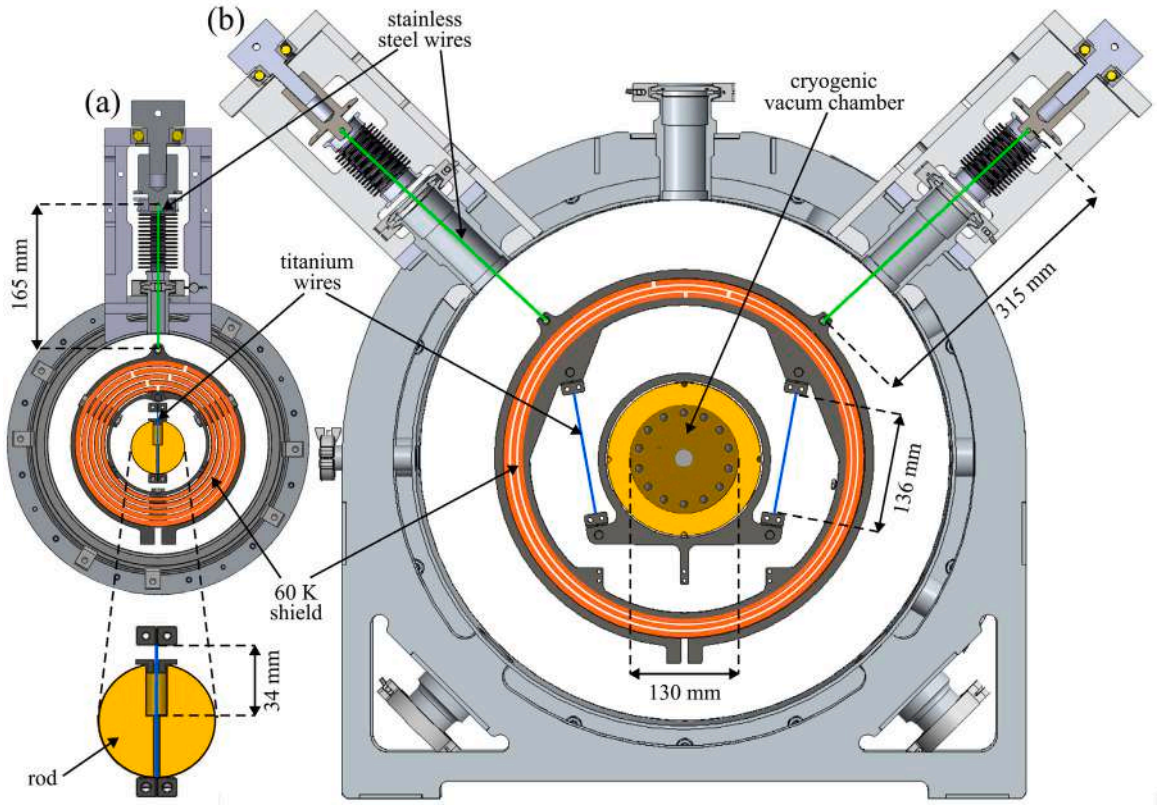

Fig. 4. Cross-sections demonstrating suspension of the first and second stages of the cryogenic system. The first-stage shields are suspended on stainless-steel wires (green lines), while the second-stage components are suspended on titanium wires (blue lines). (a) Suspension of the copper rods and their shields (the same for rods 1 and 2). (b) Suspension of the cryogenic vacuum chamber and its shield.

system is operating, thereby reducing system vibrations. The pumping speed of the cryopump is much larger than the pumping speed of the turbomolecular pump; the system reaches 1×10^{-6} Torr after 5 h of cryopumping and saturates at 2×10^{-7} Torr after 160 h, see Fig. 3.

4. Cryogenic system, the first stage

The cryogenic system has a two-layer structure. The outer layer (the first stage) serves as thermal radiation shielding, see orange parts in Figs. 1 and 2. It is thermally connected to the first stage of the cryocooler and operates at approximately 60 K. The inner layer (the second stage) consists of the cryogenic vacuum chamber and the rods that link the chamber with the second stage of the cryocooler, see the yellow parts in Figs. 1 and 2. The second stage of the cryogenic system is analysed in Section 5.

We use a commercial pulse tube cryocooler based on a closed-cycle helium system (PT-420RM by Cryomech) with a nominal cooling power of 1.8 W at T = 4.2 K at the second stage, and 50 W at T = 45 K at the first stage. In our case, the heat load at the first stage, P_{1st}, is much smaller than the nominal, hence the temperature of the cryocooler's first stage is considerably lower than 45 K. The exact relation between P_{1st} and temperature of the cryocooler's first stage, T_{1st}, is not uniquely defined, meaning, the $T_{1st}(P_{1st})$ function depends on many conditions such as the heat load of the second stage, helium pressure in the closed-cycle helium system, ambient temperature, etc. We deduce this function (assuming linear dependence in the small-P_{1st} limit) from the data points in the manufacturer's performance report, which gives

$$T_{1st} = 26.4\ \mathrm{K} + 0.26 \frac{\mathrm{K}}{\mathrm{W}} P_{1st}. \quad (1)$$

We use Eq. (1) and the measured temperature at the cryocooler's first stage, T_{1st} = 28.7 K (see the asymptotic value of the yellow curve in Fig. 3), to estimate the total heat load at the cryocooler's first stage P_{1st} = 8.8 W. This gives us an important constraint necessary to recover the heat load budget, i.e., all the heat load sources (determined in Sections 4.1, 4.2, 4.3 and 5.5) have to sum up to 8.8 W, see the '1st stage' column in Table 1.

We measure temperature at both stages of the cryogenic system with commercial diode sensors (the DT-670 diodes in the CU-HT package from Lake Shore Cryotronics) and read with a cryogenic temperature monitor (model 218S from the same manufacturer). The temperature sensors are calibrated to 8 mK for $T > 5$ K and 17 mK for $T \leq 5$ K, with the readout resolution of 1 mK. All the sensors are attached to the Cu surfaces on a thin layer of *Apiezon N* grease and attached with brass screws (brass shrinks more than copper with temperature decrease, which ensures good thermal contact down to 4 K).

4.1. Mounting conductive heat load

The thermal radiation shields are suspended on thin stainless steel stranded wires (see the green lines in Fig. 1), which well isolate the first-stage layers against the heat leakage from the room-temperature vacuum chamber. The wires are anchored to the room-temperature (approximately 295 K) holders. In Fig. 4, we show the suspending systems for the shields of rods 1 and 2, panel (a), and the cryogenic vacuum chamber, panel (b). The construction of the wire holders allows their adjustment along the wire direction (±14 mm for rod shields and ±99 mm for chamber shield) from outside the vacuum chamber via flexible vacuum bellows (the ability of making the final adjustment

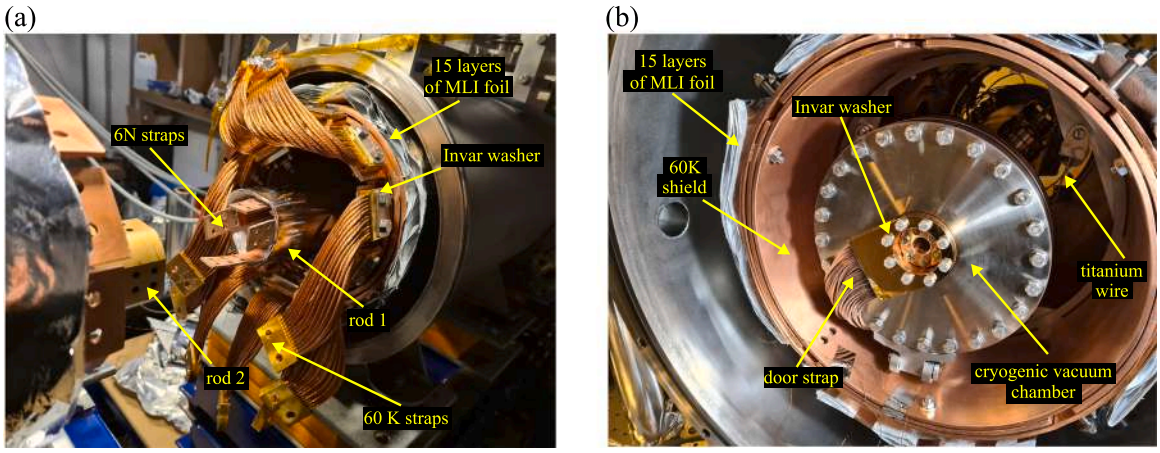

Fig. 5. Actual view of the cryogenic system. The two pictures correspond to the two panels in Fig. 4. (a) Thermal connection between rods 1 and 2, and between their thermal shields. (b) Cryogenic vacuum chamber.

from outside is critical for system assembly since all the cryogenic parts are densely packed inside the vacuum chamber with very limited access once they are installed inside). Each of the thermal shields of the rods is suspended on two vertical rods, each 2 mm in diameter and 165 mm long. The temperature difference across a wire is $\Delta T = 295\ \mathrm{K} - 60\ \mathrm{K} = 235\ \mathrm{K}$, which gives a conduction heat loss per wire of 41.9 mW, see Appendix A. The thermal shield of the cryogenic vacuum chamber is suspended on four diagonal wires. The diameter and length of each diagonal wire are 4 mm and 315 mm, respectively, which give the conduction heat loss per one diagonal wire of 87.9 mW. The exception in the thermal shield mounting is the shield of the cryocooler (left side in Fig. 1). This shield has a form of vertical cylinder, which is not suspended on wires, but supported from the bottom on four vertical titanium rods, each 2 mm in diameter and 23 mm long, which gives the conduction heat loss per one supporting rod of 173.6 mW. In total, the four supporting titanium rods and the four vertical and four diagonal stainless steel wires give the total conduction heat loss of 1.21 W.

The choice of wire diameters – 2 mm for the rod shields and 4 mm for the chamber shield – is a reasonable trade-off between conductive heat leakage and mechanical strength of the suspension wires. The total masses of the three main sections of the cryogenic system are as follows: rod 1 together with its shield amount to 75 kg, rod 2 together with its shield amount to 103 kg, and the cryogenic vacuum chamber together with its shield amount to 328 kg. The factor of safety for tensile strength of the wires is defined as a ratio of the yield strength of the suspension element material ($\sigma_{0.2} = 830$ MPa for cold-drawn AISI 304 stainless steel [40]) to the actual tensile stress, and varies from 4 to 5.5 for the suspending wires in our system. These numbers are for room temperature (295 K), which constitutes a conservative approach.

4.2. Residual gas conductive heat load

Besides the suspending wires and supporting rods, considered in Section 4.1, we should estimate also the role of heat load coming from the conduction through the residual gas. Under our conditions, we fall well into the free-molecular-flow regime, where the heat conduction through gas scales linearly with gas pressure and temperature difference, see Eq. (1.8) in Ref. [41]. For our conditions ($p = 2 \cdot 10^{-7}$ Torr $= 2.7 \cdot 10^{-5}$ Pa, $\Delta T = 235$ K, and area of the 60 K surface of 2.91 m^2) the heat load is 0.03 W. For this estimation, we conservatively assume the worst-case scenario regarding the residual gas composition, meaning we take the rate constant for H_2 (which is the largest due to small H_2 mass). For other molecules (He or N_2) the heat load is expected to be 2–4 times smaller [41].

Table 1
Heat load budget. The table summarizes all the relevant heat sources that enter the first and second stages of our cryogenic system. In the parenthesis, we indicate the sections from which the numbers come. It should be noted that the total heat load on the 2nd stage of 83 mW is a nominal engineering estimate and not a measured value.

	1st stage	2nd stage
Mounting conductive heat load	1.21 W (Section 4.1)	20.4 mW (Section 5.1)
Gas pipe conductive heat	1.1 mW (Section 5.5)	0.05 mW (Section 5.5)
Residual gas conductive heat load	0.03 W (Section 4.2)	0.17 mW (Section 5.2)
Radiative heat load	7.55 W (Section 4.3)	57 mW (Section 5.3)
Radiative heat load (direct emission from 295 K to 4 K)	–	5.4 mW (Section 5.3)
Total	8.79 W	83.02 mW

4.3. Radiative heat load

The total outer surface of the thermal shields is 2.91 m^2, which gives a black-body power absorption from 295 K-environment thermal radiation of 1250 W (429 W/m^2). Assuming a realistic emissivity of copper surfaces of $\epsilon = 0.1$ gives the radiative heat load of the first stage of the cryogenic system of 125 W, which considerably exceeds the nominal cooling power of the first stage of the cryocooler (50 W). To reduce the radiative heat load, we covered the entire outer surface of cryogenic shields with 15 layers of multilayer insulation (MLI) foil, see Fig. 5. Experimental values of thermal radiation heat flux for MLI-covered surfaces corresponding to our conditions vary in the range from 0.5 W/m^2 to 3 W/m^2 [28,30,32]. The exact value depends on many factors such as compression of layers, manufacturer, residual gas pressure, installation quality, etc. We found that a value of the thermal radiation heat flux that gives a consistent picture of the heat load budget is 2.6 W/m^2, see Table 1 (then the sum of all the predicted contributions agrees with the total heat load determined from Eq. (1)). This gives a total radiative heat load on the thermal shields of 7.55 W.

4.4. Temperature gradients

In our setup, the thermal radiation shields do not only block the room-temperature radiation heat load, but also bear large mechanical and thermal inertia (important for attenuating mechanical vibrations

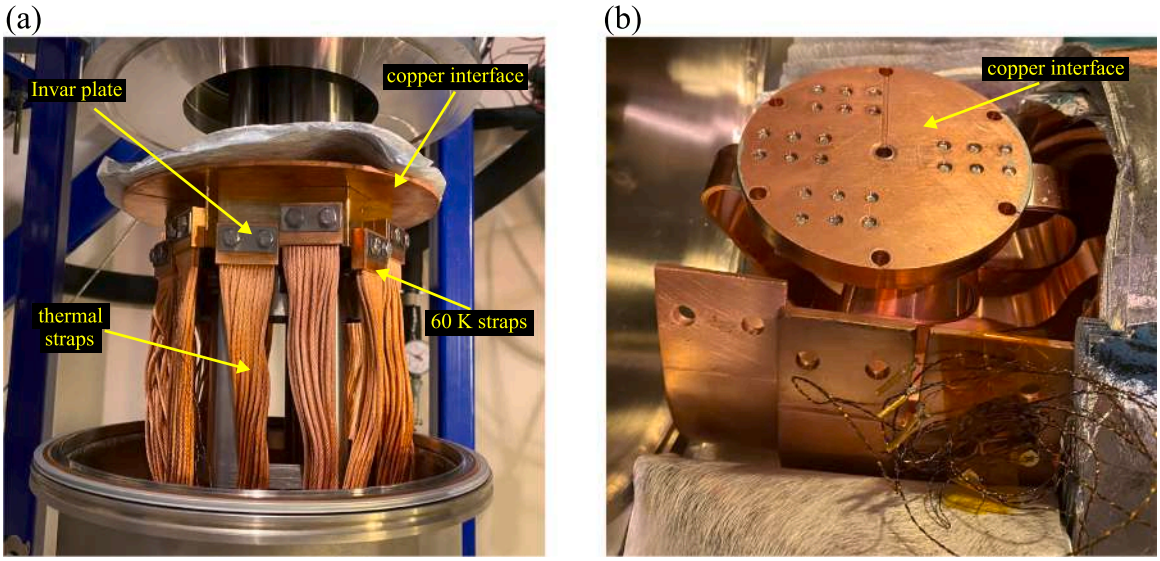

Fig. 6. Thermal connections between thermal straps and the cryocooler. (a) The first-stage thermal straps connected to a copper interface with stainless-steel screws. (b) The second-stage thermal straps connected to a copper interface with stainless-steel screws. In both cases (panels (a) and (b)), we use Invar plates to compensate for the difference in thermal expansion coefficient between copper and stainless steel. The copper blocks (for both stages) are thermally linked to the cryocooler via grease (*Apiezon N*) joints.

and temperature fluctuations), as well as play a role of thermal conductors between the cryocooler and the most distant parts of the first-stage cryogenic system. These three additional roles require the shields to be thick and massive. In this section, we provide a detailed discussion on the last of these features, i.e., thermal conductivity, and discuss the corresponding temperature gradients along the first stage.

The geometry of the thermal radiation shields is shown in Fig. 1. The thickness of the shields of rods 1 and 2 is 25 mm, while the thickness of the cryogenic vacuum chamber shield is 15 mm. We found it to be a reasonable trade-off between the highest possible inertia and thermal conductance, on the one hand, and geometrical limitations of the outer vacuum system, on the other hand. The exception is the vertical-cylinder shield of the cryocooler (left-side edge of Fig. 1) which plays only the role of blocking thermal radiation and, hence, its walls are only 5 mm thick. At the manufacturing stage, we realized that it is cheaper and easier to split the thick-wall cylinders into multi-layer structure, each 5 mm thick. We note that the thickness of the shield of rod 1 is not uniform along this axis. The number of layers on the left side is reduced to three (15 mm effective wall thickness). The reason is the mechanical stability that requires to bring the centre of the mass of the shield in between the suspending wires.

The shields are made of Electrolytic Tough Pitch copper (Cu-ETP, CW004A). All copper components were annealed after machining and bending. First the temperature of the copper components was slowly (1 h) ramped from room temperature to 800 K, then kept at 800 K for 2 h, and slowly (4 h) ramped down to room temperature. A conservative estimate of thermal conductivity in the temperature range from 30 K to 60 K is 800 W/(m K) [41] which, along with the geometry described in the previous paragraph, give thermal resistance of the shields of the rods of $R^{1st}_{R1} = 0.11$ K/W (rod 1) and $R^{1st}_{R2} = 0.07$ K/W (rod 2).

The first stage of the cryocooler and the thermal shields are connected (in series) to each other via flexible high-purity copper straps (manufactured by *Technology Applications Inc., Boulder, USA*). The straps are made from flexible copper wire based on oxygen-free high-conductivity (OFHC, 99.99% purity) copper, using *OFHC UltraFlex*^{TM} cabling. Each strap consists of 26 such wires (13 wires × 2 rows), see Fig. 5(a). Both the copper plates and the flexible wires are fabricated from OFHC copper. The manufacturer projection of thermal resistance of such strap (per 10 cm length) is 0.77 K/W at $T = 20$ K. The resistance at $T = 30$–60 K is not reported by the manufacturer explicitly, but for this purity of copper, its resistivity increases in this temperature range by approximately a factor of 1.5 [41]. Therefore, we use a value of 1.5×0.77 K/W = 1.2 K/W (per 10 cm length) for strap resistance estimations for the first stage of the cryogenic system. We subjected the copper straps to the same annealing procedure as the thermal shield (see the previous paragraph).

The cryocooler is linked to the shield of rod 1 via 12 copper straps with lengths of 25 cm (4 straps), 26 cm (4 straps), 27 cm (2 straps) and 28 cm (2 straps). The effective thermal resistance of these 12 straps (linked in parallel) is $R^{1st}_{ST1} = 0.26$ K/W. The shields of rods 1 and 2 are thermally linked via 10 copper straps, each 12 cm long (these straps are shown in Fig. 5(a)). The effective thermal resistance of these 10 straps (linked in parallel) is $R^{1st}_{ST2} = 0.14$ K/W. The shield of rod 2 is thermally linked to the shield of the cryogenic vacuum chamber via 10 copper straps with lengths of 17.5 cm (8 straps), 7.5 cm (2 straps). The effective thermal resistance of these 10 straps (linked in parallel) is $R^{1st}_{ST3} = 0.17$ K/W.

Besides the thermal resistance of copper, the effective resistances of the straps should also include resistances of the joints between the strap ends and other copper elements. Thermal conductance of copper-copper joint at 30 K–60 K temperature range is 0.03 W/K for 500 N force applied [41]. In our case, the ends of the straps are covered with gold to reduce the joint resistance, however, due to a lack of the copper-gold joint conductance data, we use a value for copper-copper joint for the present estimations (hence, the outcome of the analysis in this paragraph should be treated as conservative estimations, with expectation that actual joint resistances are smaller). Each strap at each end is attached with two M6 stainless-steel screws, see Fig. 5(a). We use Invar plates to compensate for differences in thermal expansion coefficients of copper and stainless steel, see Section 5.4 (the discussion below Eq. (5)) for details. A single screw exerts a force of 10 kN. For the R^{1st}_{ST1} case, there are 12 straps, hence 24 screws per one end, which gives a total force per one end of 240 kN. Thermal conductance of 0.03 W/K per 500 N gives 14.4 W/K for 240 kN. The corresponding resistance is 0.07 K/W per one end and 0.14 K/W for both ends. Therefore, $R^{1st}_{ST1} = 0.26$ K/W from the previous paragraph, after including the joint resistances, gets $R^{1st}_{ST1} = 0.26$ K/W + 0.14 K/W

= 0.40 K/W. The analysis for R^{1st}_{ST2} and R^{1st}_{ST3} is exactly the same except for number of straps. After including the joint resistances their values are R^{1st}_{ST2} = 0.14 K/W + 0.12 K/W = 0.26 K/W and R^{1st}_{ST3} = 0.17 K/W + 0.12 K/W = 0.29 K/W.

Finally, for the case of R^{1st}_{ST1}, we should also include a grease-connection resistance that links the entire first-stage cryogenic system with the cryocooler. The thermal straps are not directly attached to the cryocooler's first stage, because (due to cryocooler construction) one cannot apply large torque to it. For this reason, we developed a copper interface, see Fig. 6(a), to which we attach thermal straps with large force and then the entire interface is attached to the cryocooler's first stage with thermal grease (we use the *Apiezon N* grease). The interface is designed in a way to obtain the highest possible contact surface area at the joint with the cryocooler (0.0061 m^2). Based on the grease joint conductance at 30 K–60 K of 7×10^3 W/(m^2 K) [41], we estimate grease joint resistance at 0.02 K/W, hence the final value of R^{1st}_{ST1} is 0.26 K/W + 0.14 K/W + 0.02 K/W = 0.42 K/W.

To calculate the temperature gradients along the first stage of the cryogenic system, we look at it as a system of 5 thermal resistors linked in series, see Fig. 8,

$$\begin{aligned} R^{1st} &= R^{1st}_{ST1} + R^{1st}_{R1} + R^{1st}_{ST2} + R^{1st}_{R2} + R^{1st}_{ST3} \\ &= (0.42 + 0.11 + 0.26 + 0.07 + 0.29)\ \text{K/W} \\ &= 1.15\ \text{K/W}. \end{aligned} \tag{2}$$

In principle, to calculate the temperature difference between the first stage of the cryocooler and the shield of the cryogenic vacuum chamber, one would need to carefully decompose the total heat load, P_{1st} = 8.8 W, into several branches that enter the resistance series (Eq. (2)) in different nodes. However, when we aim at simple physical picture (with few tens of percent accuracy being sufficient for this analysis), we can approximate it with half of the total thermal power, $P_{1st}/2$ = 4.4 W, propagating through all the resistors in series, which gives the temperature difference across the entire first stage of

$$\Delta T_{1st} = R_{1st}\frac{P_{1st}}{2} = 5.1\ \text{K}. \tag{3}$$

The actual, directly measured, value of the temperature difference across the first stage of the cryogenic system is ΔT_{1st} = 57.9 K − 28.7 K = 29.2 K, which is considerably larger than the value based on our best estimations of resistance and heat load, Eq. (3). This discrepancy cannot be explained by underestimated value of P_{1st}. Six times larger total heat load on the first stage of the cryocooler will induce much larger temperature on it than the measured T_{1st} = 28.7 K, see Eq. (1). Therefore, our conclusion is that the thermal resistance is underestimated. The most difficult to estimate contributions to R_{1st} are resistances of solid–solid joints. They depend on many factors that are problematic to be uniquely determined in actual realization such as forces applied, thickness of grease layer, surface quality, etc. To explain the ΔT_{1st} deviation, the total thermal resistance should be R_{1st} = 29.2 K/4.4 W = 6.6 K/W instead of 1.15 K/W determined in Eq. (2).

5. Cryogenic system, the second stage

The structure of this section is similar to the structure of Section 4, but concerns the second stage of the cryogenic system. In the first three subsections, Sections 5.1–5.3, we provide a detailed discussion on conductive and radiative heat loads. In Section 5.4, we analyse the temperature gradient along the second stage. Finally, in Section 5.5, we provide a detailed discussion on design and properties of the cryogenic vacuum chamber, a key part of the entire system.

First, however, we describe the characteristics of the cryocooler's second stage and use them to estimate its total heat load P_{2nd}. In our case, when the system is cooled down (all the heaters are off and the second stage reached the lowest temperature) the heat load at the second stage, P_{2nd}, is much smaller than the cryocooler's nominal cooling power, hence the temperature of the cryocooler's second stage is considerably lower than the nominal 4.2 K. Similarly to the first stage, see Section 4, the exact relation between P_{2nd} and the temperature of the cryocooler's second stage, T_{2nd}, is not uniquely defined, meaning, the $T_{2nd}(P_{2nd})$ function depends on many conditions such as heat load of the first stage, helium pressure in the closed-cycle helium system, ambient temperature, etc. We deduce this function (assuming linear dependence in the small-P_{2nd} limit) from the measurement points from the manufacturer performance data report, which gives

$$T_{2nd} = 2.25\ \text{K} + 1.3\frac{\text{K}}{\text{W}}P_{2nd}. \tag{4}$$

We use Eq. (4) and the measured temperature at the cryocooler's second stage, T_{2nd} = 3.6 K, to estimate the total heat load at this stage, P_{2nd} = 1.0 W. Note that the asymptotic value of T_{2nd} (blue curve in Fig. 3) has not yet fully converged within the time range; it reaches 3.79 K at the largest times shown, whereas it asymptotically approaches approximately 3.6 K. This asymptotic value depends on multiple factors and may vary by up to 0.1 K in practice, which gives an estimation of P_{2nd} = 1.0 W uncertainty of 0.1 W. Note that this estimation of the P_{2nd} uncertainty is based on Eq. (4), which itself is just an approximation based on manufacturer performance data report and (as outlined above) depends on many external conditions. Therefore, the expected total combined uncertainty of P_{2nd} is much larger than 0.1 W.

5.1. Mounting conductive heat load

The cryogenic rods (the rods that link the second stage of the cryocooler with the cryogenic vacuum chamber, see rods 1 and 2 in Fig. 1) are suspended on thin titanium wires. Each of the two rods is suspended on two titanium wires (see Fig. 1), 1 mm in diameter and 34 mm long, see Fig. 4. The cryogenic vacuum chamber is suspended on four inclined titanium wires, each 2 mm in diameter and 136 mm long, see Fig. 4. All these suspending titanium wires are depicted in Figs. 1 and 4 as blue lines.

From the perspective of thermal-conduction analysis, each titanium wire can be seen as a thermal conductor anchored between 60 K and 4 K temperatures. Conduction heat loss is 2.55 mW per wire for rod suspension and 2.55 mW per wire for cryogenic vacuum chamber suspension, see Appendix A (this is a coincidence that for the two different-geometry cases the heat loss per wire is the same). This gives a total conductive heat load through all the suspending wires of 20.4 mW.

The choice of wire diameters – 1 mm for the rod suspensions and 2 mm for the chamber suspension – is a reasonable trade-off between conductive heat leakage and mechanical strength of the titanium suspension wires. Grade 5 titanium (Ti–6Al–4V) was selected for its favourable combination of low thermal conductivity at cryogenic temperatures and high tensile strength [42]. The total masses of the three main sections of the second stage of the cryogenic system are as follows: rod 1 amounts to 17 kg, rod 2 amounts to 22 kg, and the cryogenic vacuum chamber together with ancillary equipment amounts to 127 kg. The factor of safety for tensile strength of the wires is defined as a ratio of the yield strength of the suspension element material ($\sigma_{0.2}$ = 1.6 GPa for Grade 5 titanium [42]) to the actual tensile stress, and varies from 6.4 to 8.2 for the suspending titanium wires in our system. These numbers are for room temperature (295 K), which constitutes a conservative approach.

5.2. Residual gas conductive heat load

We estimate the role of heat load on the second stage coming from the conduction through the residual gas in the same way as we did for the case of the first stage of the cryogenic system, see Section 4.2. It is difficult to estimate the pressure between the 60 K and 4 K layers, but we know that it should be much smaller than the readout of the room-temperature pressure gauge. For the purpose of the present estimations, we conservatively assume it to be one order of magnitude smaller,

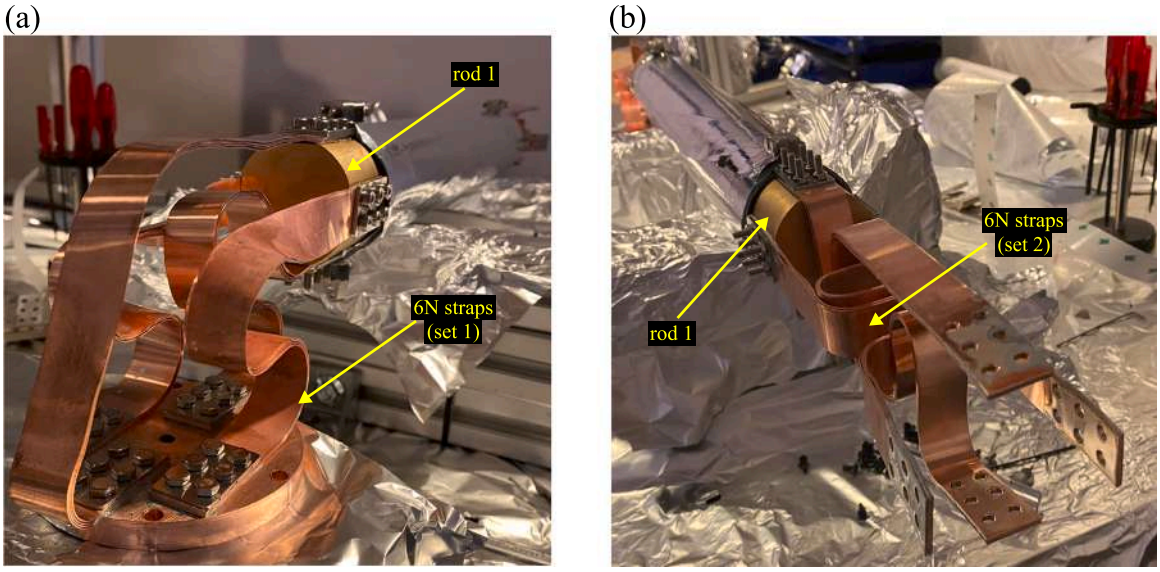

Fig. 7. A complete set of thermal straps at the two sides of rod 1. (a) The connection with the copper block to be linked to the second stage of the cryocooler. (b) Thermal straps to be linked to rod 2.

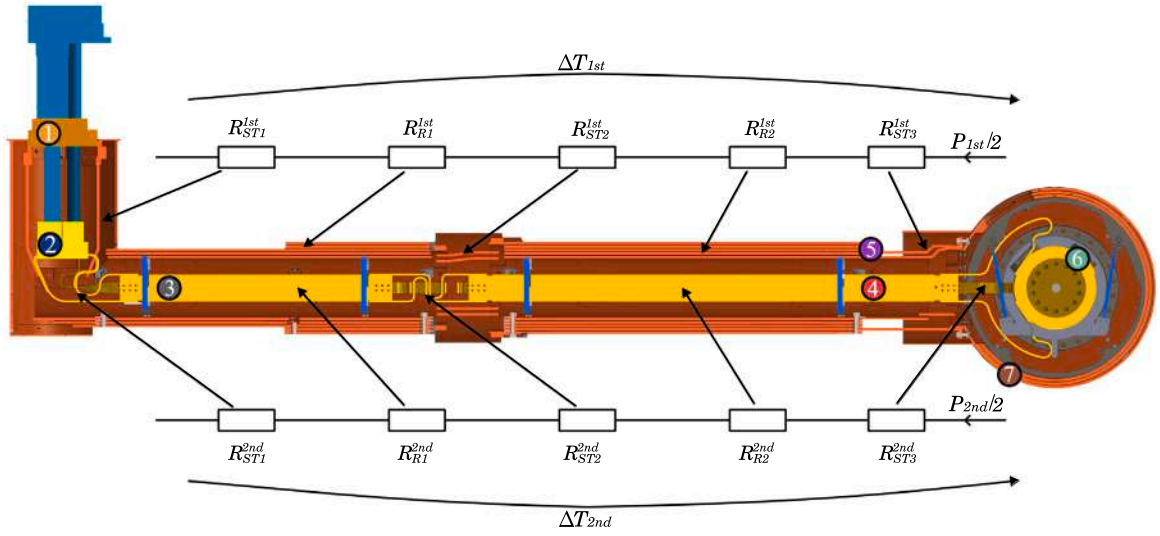

Fig. 8. The contributions to the thermal resistances between the cryocooler and the cryogenic vacuum chamber. The upper chain of resistors corresponds to the first stage of the cryogenic system (the link between the first stage of the cryocooler and the shields of cryogenic vacuum chamber); it illustrates the meaning of Eq. (2). The lower chain of resistors corresponds to the second stage of the cryogenic system (the link between the second stage of the cryocooler and the cryogenic vacuum chamber); it illustrates the meaning of Eq. (8).

$p = 2.7 \cdot 10^{-6}$ Pa. Using Eq. (1.8) from Ref. [41] (the same approach as in Section 4.2) for $\Delta T = 56$ K, and area of the 4 K surface of 0.77 m^2, we get the heat load of 0.17 mW. Again, as in Section 4.2, we conservatively take the rate constant for H_2.

5.3. Radiative heat load

The total outer surface of the second-stage part of the cryogenic system is 0.77 m^2 (the contribution from rods 1 and 2 is 0.28 m^2, while the contribution from the cryogenic vacuum chamber is 0.49 m^2). This gives a black-body power absorption from the 60 K-shields thermal radiation of 566 mW (735 mW/m^2). Assuming a realistic emissivity of copper surfaces of $\epsilon = 0.1$ gives the radiative heat load of the second stage of the cryogenic system of 57 mW.

On the one hand, the 57 mW value may be overestimated because we did not consider the presence of the MLI foil for the rods, see Figs. 5(a) and 7 (the cryogenic vacuum chamber is not covered with the MLI foil). On the other hand, the 57 mW value may be underestimated because we neglected the area of the thermal links and cryocooler 4 K finger. We note, however, that these two simplifications have smaller impact than the uncertainty of the assumed $\epsilon = 0.1$ whose actual value may differ from the assumed one by a factor of 2.

One should also note that the optical access to the cryogenic vacuum chamber (along the chamber axis, see Fig. 2) entails additional heat load due to a direct line of sight between the second stage of the cryogenic system and the room-temperature environment. The two on-axis apertures in the 60-K shields have diameters of 20 mm. A power of thermal radiation that would enter through such two apertures is

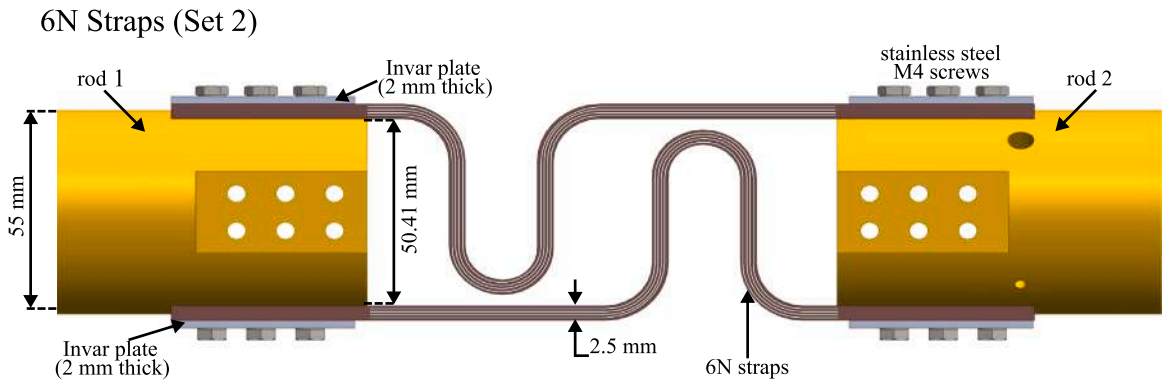

Fig. 9. Detailed picture of the thermal connection between rods 1 and 2, 6N straps (set 2). For clarity of the picture, only two of the four thermal straps are shown. The 2.5 mm thickness of the straps means that there are 5 layers, 0.5 mm each.

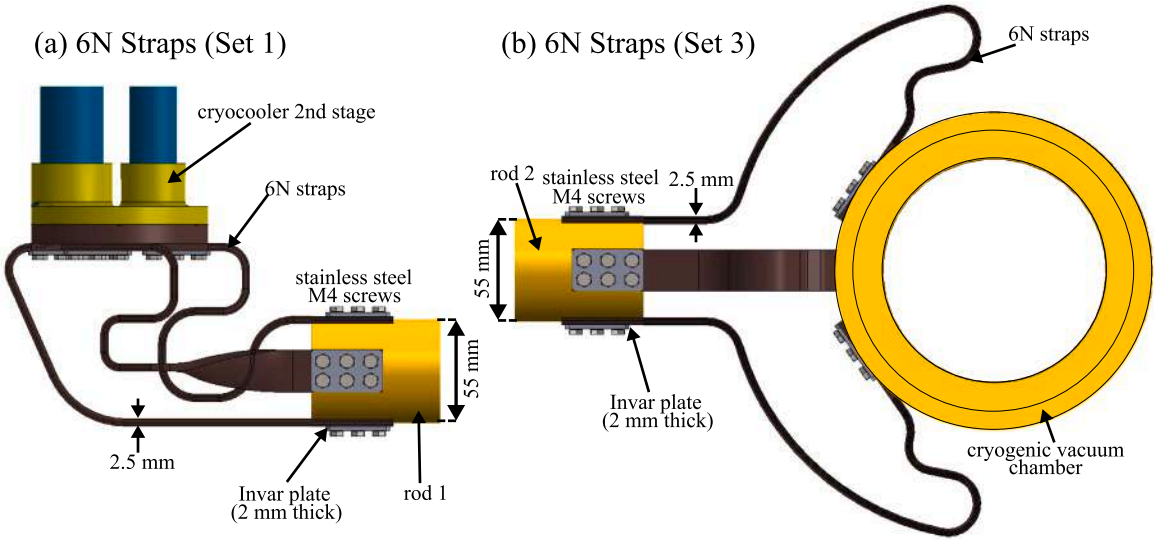

Fig. 10. Thermal connection between cryocooler and rod 1, 6N straps (set 1). For clarity of the picture, only three of the four thermal straps are shown. (b) Thermal connection between rod 2 and the cryogenic vacuum chamber, 6N straps (set 3). For clarity of the picture, only three of the four thermal straps are shown. The 2.5 mm thickness of the straps means that there are 5 layers, 0.5 mm each.

270 mW. Assuming, conservatively, $\epsilon = 0.2$, this would give additional heat load of 54 mW, which would nearly double the total heat load on the second stage, see Table 1. To avoid it, we introduced a 60 K-pipe at each aperture directed along the chamber axis (20 mm in diameter, and 50 mm long) that reduce the clearance solid angle by a factor of 100. However, due to small emissivity of copper much of the thermal radiation will be reflected from the inner surfaces of these pipes and we estimate that the reduction factor will be an order of magnitude smaller, i.e., at the level of 10, which gives 54 mW/10 = 5.4 mW heat load coming from the room-temperature environment.

5.4. Temperature gradients

Similarly to the first stage of the cryogenic system, the components of the second stage play several roles in the system with their large masses being beneficial. First, the large thermal and mechanical inertia are important for attenuating temperature fluctuations and mechanical vibrations that come both from the cryocooler oscillations and external perturbations. Second, the large masses entail large cross-sections that are important for ensuring high thermal conductivity. In this section, we provide a detailed discussion on the last of these features, i.e., thermal conductivity, and discuss the corresponding temperature gradients along the second stage.

The geometry of the second stage of the cryogenic system is shown in Fig. 1 as the yellow components. The cryogenic vacuum chamber (right side of the figure) is thermally connected to the second stage of the cryocooler (left side of the figure) via two heavy copper rods (rods 1 and 2 in Fig. 1). The rods have a form of solid cylinders, 55 mm in diameter. The lengths of the rods are 55 cm (rod 1) and 100 cm (rod 2). They are made of high-purity copper (5N5) and annealed (the same annealing process as described in Section 4.4). The corresponding thermal conductivity at 4 K is expected to be better than 10^4 W/(m K) [41], which gives thermal resistances of rods 1 and 2 of $R^{2nd}_{R1} = 0.023$ K/W and $R^{2nd}_{R2} = 0.042$ K/W, respectively.

In contrast to the first stage of the cryogenic system (operating at 60 K), thermal straps providing sufficiently high conductance at 4 K were not available commercially (the copper purity of the commercial

straps was not sufficiently high). For this reason, we used custom made straps based on 6N copper tape, 0.5 mm thick and 20 mm wide. There are three sets of thermal straps in the second stage of our cryogenic system. Set 1 links the second stage of the cryocooler with rod 1, set 2 links the two rods, and set 3 links rod 2 with the cryogenic vacuum chamber, see Fig. 1. Each set consists of four thermal straps and each thermal strap consists of five tapes linked in parallel, see Figs. 7, 9 and 10. Within a single strap the tapes are soldered at the strap ends with indium solder (the thermal resistance of indium solder connections is very small [41], and it is negligible compared to other resistance contributions present in our setup). The lengths of the straps are: 29 cm, 27 cm, and two times 20 cm (set 1); two times 26 cm and two times 29 cm (set 2); two times 36 cm and two times 37 cm (set 3). Each thermal strap is bent in several places to ensure mechanical flexibility of the connection, see Figs. 7, 9 and 10. Additionally, the annealing process (the same as described in Section 4.4), besides its main role of improving thermal conductivity, considerably increases the flexibility of the straps.

For the annealed 6N copper, we can conservatively take the value of thermal conductivity at $T = 4$ K as $1.5 \cdot 10^4$ W/(m K) [41]. This gives thermal resistances of the sets 1–3 of 0.08 K/W, 0.09 K/W, and 0.12 K/W, respectively.

Besides thermal resistivity of copper, to estimate the strap connection resistance, we should also consider the contribution from the joints between solid surfaces. There are two strategies for making low-resistance joints. The first is to apply strong force (without grease), the second is to use large joint area (with grease); the second one is typically used in cases when a strong force cannot be applied. In this paragraph, as an example, we provide a detailed discussion for the case of thermal strap set 2 (the straps between rods 1 and 2). For this case, we apply the first strategy (we apply strong force). The ends of the rods are covered with gold, while the ends of the straps are covered with indium. Due to the lack of literature data for this specific material combination (indium-gold joint), we take the thermal conductance for the closest one available in the literature, i.e. indium-copper, as a conservative estimation (replacing copper with gold should increase conductance). At 4 K the indium-copper conductance is 4×10^{-3} W/K for 100 N applied force and scales linearly with force [41]. Per each rod end, we installed 12 stainless steel M4 screws, see Fig. 7(b). Each screw was tightened to a torque of 4 Nm, which gives a force per screw of 8.3 kN. Therefore, a total effective force per one end of a rod is 200 kN (each screw exert force on thermal straps from two sides, hence for 12 screws there are 24 clamping points), which gives thermal conductance of 8 W/K or, equivalently, the resistance of 0.12 K/W. The thermal strap set 2 consists of two such resistances plus the thermal resistivity of copper determined in the previous paragraph, which gives the total resistance of set 2 of

$$R^{2nd}_{ST2} = (2 \cdot 0.12 + 0.09)\ \text{K/W} = 0.33\ \text{K/W}. \tag{5}$$

At this point, we should also carefully consider the difference in thermal expansion coefficient between copper and stainless steel. The copper rod and straps shrink more than stainless-steel screws do when temperature decreases, and without any additional efforts the screws would come loose, and the resistance of the joint would increase dramatically. To avoid this, we introduce Invar plates which compensate for the difference in thermal expansion coefficient, see Figs. 9 and 10. The thermal expansion coefficient of Invar is much smaller comparing to copper and stainless steel, and even a thin layer of Invar (see Figs. 9 and 10) suffices to compensate for the difference, see Appendix B. We adopt the same approach based on Invar plates for all the other thermal joints adjusting the thickness of Invar to the thickness of copper.

The analysis for set 3 is conceptually the same. The resistance of the solid–solid joint from the rod 2 side is exactly the same as in the set 2 case, i.e., 0.12 K/W. The resistance of the solid–solid joint from the cryogenic vacuum chamber side is 0.20 K/W (due to technical and system-geometry limitations the applied force is smaller comparing to the other side of the strap set). The total resistance of set 3 is

$$R^{2nd}_{ST3} = (0.12 + 0.20 + 0.12)\ \text{K/W} = 0.44\ \text{K/W}, \tag{6}$$

with the first two contributions coming from the solid–solid joints and the last contribution coming from copper resistance.

For set 1, the total-resistance analysis contains one more contribution. The thermal straps are not directly attached to the cryocooler's second stage because, due to cryocooler construction, one cannot apply large torque to it. For this reason, we developed a copper interface, see Fig. 6(b), to which we attach thermal straps with large force and then the entire interface is attached to the cryocooler's second stage with thermal grease (we use the *Apiezon N* grease). The interface is designed in a way to obtain the highest possible contact surface area at the joint with the cryocooler (68 cm^2). Based on the grease joint conductance at 4 K reported in [43], 947 W/(m^2 K) (similar value is reported in Ref. [41]), we estimate grease joint resistance at 0.15 K/W. The total resistance of set 1 is

$$R^{2nd}_{ST1} = (0.20 + 0.12 + 0.08 + 0.15)\ \text{K/W} = 0.55\ \text{K/W}, \tag{7}$$

with the first two contributions coming from the solid–solid joints, the third contribution coming from copper resistance, and the last one from the grease joint resistance.

To calculate the temperature gradients along the second stage of the cryogenic system, we look at it as a system of 5 thermal resistors linked in series, see Fig. 8,

$$\begin{aligned} R^{2nd} &= R^{2nd}_{ST1} + R^{2nd}_{R1} + R^{2nd}_{ST2} + R^{2nd}_{R2} + R^{2nd}_{ST3} \\ &= (0.55 + 0.02 + 0.33 + 0.04 + 0.44)\ \text{K/W} \\ &= 1.38\ \text{K/W}. \end{aligned} \tag{8}$$

Following the same approximate approach as in Section 4.4, to have a reasonable estimate of temperature difference along the second stage of the cryogenic system, we approximate the full picture with half of the total thermal power, $P_{2nd}/2$, propagating through all the resistors in series, R^{2nd}, which gives the temperature difference across the entire second stage of

$$\Delta T_{2nd} = R_{2nd} \frac{P_{2nd}}{2} = 0.69\ \text{K}, \tag{9}$$

with $P_{2nd} = 1.0$ W taken from the analysis of cryocooler heat load at the second stage, see Eq. (4) and the discussion below it. The predicted temperature difference of 0.69 K agrees well with the actual measured value of 0.83 K. Note that the corresponding curves in Fig. 3 in the shown time range do not cover the converged temperature limits (for the largest time shown in Fig. 3 the difference between curves 6. and 2. is 1.15 K, while the fully converged temperature difference is 0.83 K).

One should note a significant discrepancy between P_{2nd} estimated from the analysis of the cryocooler heat load at the second stage (Eq. (4)), which gives $P_{2nd} = 1.0$ W, and P_{2nd} determined from our best understanding of the budget of the heat sources in our system, which gives $P_{2nd} = 83$ mW, see Table 1. At the present stage of the setup development, we are not able to conclusively resolve this discrepancy. Most likely, majority of this discrepancy should be attributed to the approximate nature of Eq. (4). This means that most likely the actual value of P_{2nd} is much smaller than 1 W and it is closer to 83 mW as it follows from the budget of the heat sources (Table 1). The estimations in the 2nd-stage row in Table 1 are well justified and even if we take, for instance, extreme value of emissivity of copper surfaces of $\epsilon = 0.2$ (instead of $\epsilon = 0.1$ taken for Table 1 estimations) this would results in $P_{2nd} = 140$ mW, which is still much smaller than 1 W. Note also that the conclusions from the dynamic response analysis and the corresponding RC-filter modelling (see Section 6) suggest that the actual value of R^{2nd} is approximately one order of magnitude larger than the value determined in this section (Eq. (8)), which makes $P_{2nd} = 83$ mW much more consistent with the measurement of the temperature difference across entire second stage. To sum up, different types of measurements and

estimations that were possible to perform for our system give a large scatter of P_{2nd} value ranging from 83 mW to 1 W, but a holistic view makes a more consistent picture of different source of information when P_{2nd} is at the level of 100 mW. We plan to install additional temperature sensors on both stages of the cryogenic setup and schedule additional measurement campaigns deliberately aimed at better understanding the heat loads and thermal resistances. Although, the present performance of our setup is already sufficient to address important scientific and metrological challenges [39], the setup does have a large potential for further improvements in terms of the lowest possible temperature we can reach. If we manage to reach the actual heat load and resistance at the estimated levels of 82.9 mW and 1.38 K/W then we will be able to cool down the cryogenic chamber well below 4 K, which will open new research opportunities for this experimental platform.

5.5. Cryogenic vacuum chamber

The axial cross-section of the cryogenic vacuum chamber is shown in Fig. 2. The chamber has a form of a thick-wall copper cylinder. The unique features of the cryogenic vacuum chamber are its large dimensions (the inner diameter and length of the cryogenic chamber are 120 mm and 785 mm, respectively; a volume of 8.9 l) and thickness of its walls (25 mm). Thick walls ensure exceptionally low temperature gradients across the entire chamber and large thermal and mechanical inertia, which are beneficial for damping mechanical vibrations and temperature fluctuations. The chamber weighs 127 kg, out of which 83 kg comes from the copper cylinder and copper doors.

To meet the high-vacuum requirements, we use the CF flanges. At the two ends of the cylinder, we installed large, CF200, stainless-steel flanges. We customized the flanges to connect them with the copper cylinder and copper doors, see Fig. 2. The connections between the steel CF flanges and copper cylinder and doors are sealed with indium wires and tested to endure temperature cycling between room temperature and 4 K. For the CF flanges, we use the standard copper gaskets; we tested that they endure temperature cycling in the full temperature range. The cryogenic vacuum chamber has an on-axis optical access sealed on both sides with sapphire windows WG31050-D sapphire windows from ThorLabs) and indium gaskets, see Fig. 2. We use sapphire because it has high thermal conductivity at deep cryogenic conditions (more than three orders of magnitude higher than typical glasses) and block thermal radiation.

The cryogenic vacuum chamber is equipped with four CF40 flanges (two of them are seen in Fig. 2), three of them are used for electric feedthroughs and one for gas feedthrough. The gas feedthrough is connected to a long (3 m) and thin (2.5 mm and 3.2 mm in inner and outer diameters, respectively) stainless-steel pipe that links the cryogenic vacuum chamber with the room-temperature valve outside the outer vacuum chamber. This allows us to evacuate and fill in the cryogenic vacuum chamber with a gas sample even when the system is cooled to deep cryogenic temperatures. To reduce the heat load at the second stage, the pipe is thermally anchored at half its length to the thermal shields (60 K). The pipe length from 4 K to 60 K is 1.5 m, and the length from 60 K to room temperature is 1.5 m, which give conductive heat loads of 1.1 mW and 0.05 mW at the first and second stages, respectively (note that stainless steel is a good thermal isolator, especially at cryogenic temperatures).

5.5.1. Temperature gradients across the cryogenic vacuum chamber

The cryogenic vacuum chamber is made from pure (4N5) and annealed copper which gives thermal conductivity higher than 4000 W/(m K) at $T = 4$ K [41]. The wall thickness is 25 mm, which together with the high thermal conductivity gives enormous thermal conductance. To calculate temperature gradients at the cryogenic vacuum chamber, we need to estimate the magnitude of the heat flow along the chamber walls. Out of the total heat load at the second stage of the cryogenic system of 83.02 mW, see Table 1, 51.6 mW comes from the cryogenic vacuum chamber, with 10.2 mW coming from the mounting conductive heat load, 36 mW from radiative heat load, and 5.4 mW from direct emission from 295 K to 4 K.

For the simplest conservative estimation of temperature gradient along the surface of the cryogenic vacuum chamber, we assume that the entire heat load (51 mW) enters at the opposite side of the chamber cylinder with respect to the thermal straps. Then the cylindrical wall of the chamber can be seen as two thermal resistors (linked in parallel) each 227 mm long and having a cross-section of 25 mm × 785 mm = 0.02 m^2. The resistance of each of the two resistors at 4 K is

$$R = \frac{0.227\ \text{m}}{4000\ \frac{\text{W}}{\text{Km}} \times 0.02\ \text{m}^2} = 2.9 \times 10^{-3}\,\frac{\text{K}}{\text{W}}. \tag{10}$$

This gives an estimation of temperature uniformity along the chamber cylinder of $\Delta T = R \times P/2 = 74\ \mu$K. It should be noted that the copper doors (at both sides of the chamber) are not directly thermally linked to the copper cylindrical chamber (they are thermally isolated by the stainless-steel CF flanges). To ensure thermalization of the copper doors with the main cylinder, we use flexible copper straps (one strap per each door, see Figs. 2 and 5(b)). This solution gives us a flexibility of opening and closing the CF flanges without the need of remaking the thermal connection at every closing. Each strap is 330 mm long and is composed of 52 *OFHC UltraFlex™ Cabling* flexible copper wires (26 wires × 2 rows). This gives estimated thermal resistance at 4 K (per strap) of 5.9 K/W. The thermal radiation heat load (coming from the 60 K shields) per each door is 3.6 mW, which gives temperature difference between the doors and the main cylinder of 21 mK.

For the application demonstrated in Ref. [39], the 21 mK difference at the chamber doors is fully sufficient for the project requirements; note that in Ref. [39] the optical cavity is thermally anchored to the chamber cylinder and the slight temperature difference at the doors hardly influence the optical cavity. Nonetheless, we note that if needed, the 21 mK temperature difference can be easily reduced by more than order of magnitude by covering the doors with MLI foil.

6. Temperature oscillation attenuation

In Section 5, we performed a detailed analysis of the heat loads on the second stage of the cryogenic system, the resistances between the cryocooler's second stage and the cryogenic vacuum chamber, and the corresponding temperature gradients to construct a consistent description of the stationary state of the system when the cryogenic vacuum chamber reaches the lowest temperature of 4.9 K. In this section, we extend this analysis to include a dynamical response of the system and describe the attenuation of temperature fluctuations generated by the cryocooler.

In the simplest approach, we can approximate our setup with a simple series RC circuit, see Fig. 11(a), with R and C being thermal resistance and capacity, respectively. Note that there is a full equivalence between the ordinary electric series RC circuit and a thermal system composed of thermal resistor and thermal capacitor. The units of thermal resistance and capacity are K/W and J/K (instead of Ω and F for their electric counterpart), respectively, but the unit of the time constant, $\tau = RC$, is second, the same as for the electric RC circuit.

We take C as the heat capacity of the cryogenic vacuum chamber (the heat capacity of the rods is negligible at this level of approximation). The cryogenic vacuum chamber is composed of 83 kg of copper and 42 kg of stainless steel. Interestingly, at T ranging from 4 K to 5 K, the specific heat of stainless steel is over an order of magnitude larger compared to copper (0.12 J/(kg K) [44] for copper and 2.5 J/(kg K) [45] for stainless steel), and despite its smaller mass, stainless steel gives a much larger contribution to the overall heat capacity of the cryogenic vacuum chamber (10 J/K for copper and 105 J/K for stainless steel), which gives the overall effective heat capacity for our system of $C = 115$ J/K.

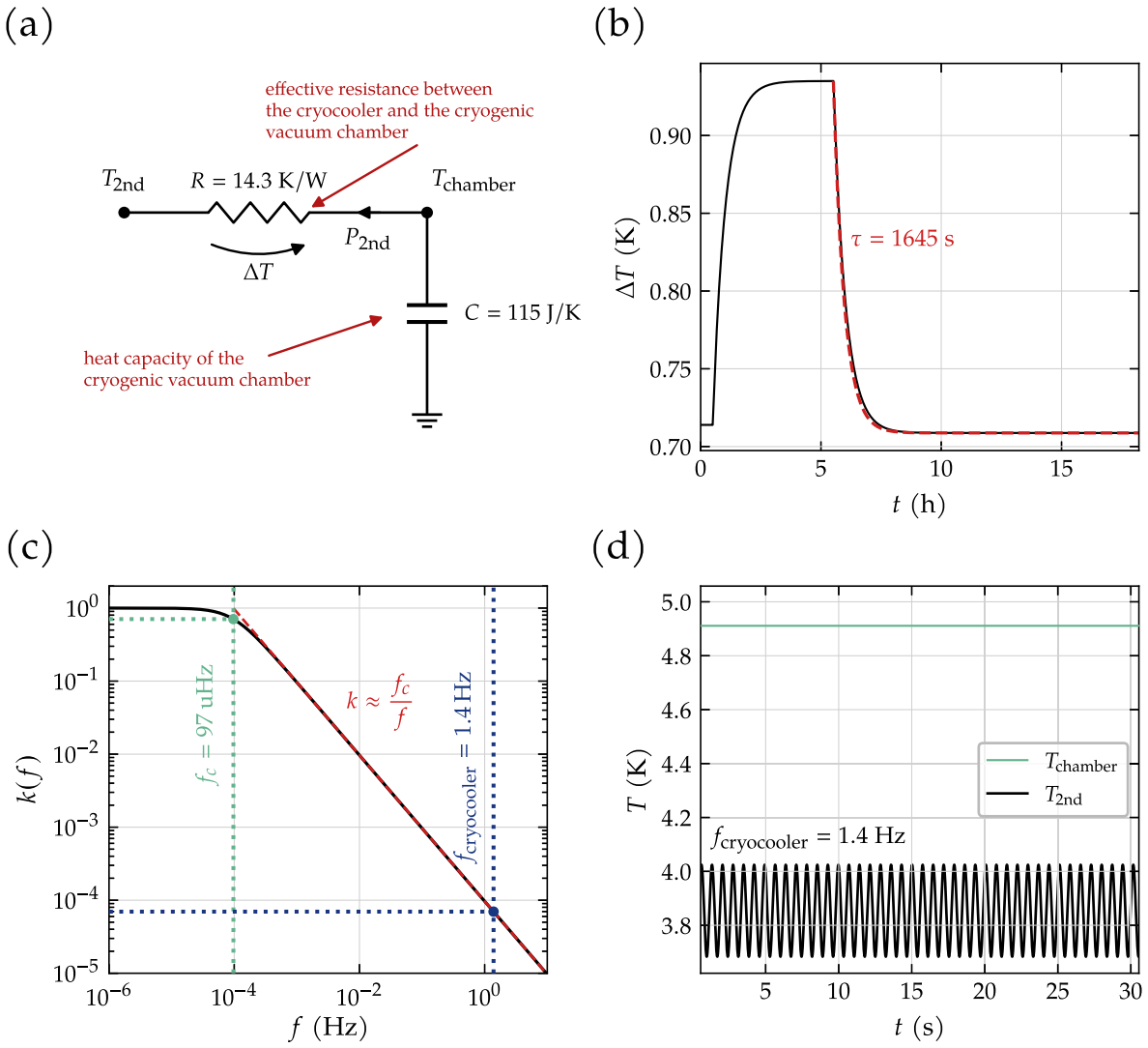

Fig. 11. Attenuation of thermal oscillations. (a) Simple RC model of our system. (b) System response to a step excitation. The black solid line is the experimental measurement (sensor 6 in Fig. 1). The dashed red line is a fit of an exponential function to the decay part of the temperature step. (c) Attenuation of the temperature oscillation (between cryocooler's second stage and the cryogenic vacuum chamber) as a function of the oscillation frequency. The black solid line is the RC-model attenuation dependence, while the red dashed line is the $k \approx f_c/f$ asymptotic ($f \gg f_c$) behaviour. (d) Temperature oscillation at the cryocooler's second stage and the cryogenic vacuum chamber.

The most straightforward way to identify R in our simplified approach is to take the total resistance between the second stage of the cryocooler and the cryogenic vacuum chamber, R^{2nd}, estimated by Eq. (8) at $R^{2nd} = 1.38$ K/W. This gives the RC time constant of $\tau = RC = 115$ J/K $\times$ 1.38 K/W = 159 s, which is considerably smaller than the experimentally determined value of 1645 s, see Fig. 11(b). This discrepancy means that the value of the effective resistance is considerably underestimated; its value should be $R = 1645$ s/(115 J/K) = 14.3 K/W (note that the value of C is robust since the thermal inertia is simply determined by the mass of the cryogenic vacuum chamber). The simplest solution to this discrepancy would be to conclude that Eq. (8) underestimates R^{2nd} by an order of magnitude (this would also explain a part of the discrepancy in the predicted and measured P_{2nd}, see the discussion in the last paragraph in Section 5.4). Most likely, the underestimated value of R^{2nd} gives the major contribution to the RC time discrepancy, however, this is not the only part of the explanation. The other part is related to the structure of the cryogenic vacuum chamber, i.e., the thermal resistances within the cryogenic vacuum chamber are not negligible. First, the copper doors and part of the stainless-steel CF flanges are linked with the main copper cylinder via thermal straps of non-negligible resistances. Second, thermal resistivity of stainless steel at 4 K is nearly five orders of magnitude larger than resistivity of high-purity copper and the stainless-steel components cannot be simply treated as heat capacitors (as it can be done for copper elements) but rather as a complex thermal RC structures with continuous distribution of resistance and capacity (despite large cross section and small length of the stainless-steel components, their resistance is not negligible due to the enormous resistivity). The detailed modelling of thermal resistance and capacity distribution of such complex structures is beyond the scope of this work (at this stage, we also lack a sufficient number of temperature measurement points to experimentally validate such simulations).

In order to describe the attenuation of the cryocooler's temperature fluctuations, we use the simple RC filter model and identify the corresponding time constant with the experimentally determined decay time $\tau = 1645$ s, see Fig. 11(b), which gives the cutoff frequency of $f_c = 1/(2\pi\tau) = 97$ μHz. In Fig. 11(c), we show the corresponding attenuation of the RC filter, k, as a function of the frequency of thermal fluctuations, f. In the limit of $f \gg f_c$, the RC filter attenuation can be expressed as $k \approx f_c/f$. The frequency of the cryocooler oscillations is $f = 1.4$ Hz, hence for our system $k = 6.9 \times 10^{-5}$. The amplitude of cryocooler's oscillations at the second stage is 0.35 K, hence the amplitude of temperature oscillations at the cryogenic vacuum chamber expected from the simple RC-filter model is 24 μK. This is consistent with our measurement, see Fig. 11(d), the amplitude of temperature oscillations at the cryogenic vacuum chamber is below 1 mK, which is the resolution of our temperature metre. The exceptionally low level of temperature fluctuations, achieved this way, is sufficient to address the most demanding metrological applications in the deep cryogenic regime as recently demonstrated in Ref. [39].

7. Mechanical noise attenuation

Mechanical noise attenuation is another important aspect of cryogenic platforms employing optical cavities. A comprehensive quantitative analysis of vibration transfer and suppression mechanisms is, however, beyond the scope of the present work; detailed studies of cryogenic vibration isolation and cryocooler-induced disturbances can be found in the literature, e.g. [33–35]. From the perspective of applications in high-precision cavity-enhanced spectroscopy, the important feature to study is how much the mechanical noise generated by the cryocooler propagates to the optical cavity and induces its length fluctuations. The best detector to quantitatively characterize such fluctuations is the optical cavity itself (we used the optical cavity shown in Fig. 1 in Ref. [39]). A quantity that can be used to express the level of cavity length fluctuations is the error signal which actively drives the seed laser (see Fig. 1 in Ref. [39]). To calibrate such measurement and obtain an absolute unit of length fluctuations (metre), we modulated the cavity length with piezo mirror position actuator [46] and measured the error signal response. The measured peak-to-peak amplitude of the error signal voltage translates to the peak-to-peak cavity length fluctuations of 2 nm. However, what is the most important in this measurement is that we do not see any meaningful difference in this fluctuation level between having cryocooler turned on and off. This confirms our prediction that the majority of the error signal amplitude do not come from the cavity length fluctuations but from the laser frequency noise. Therefore the above reported value of cavity length fluctuations of 2 nm should be understood as a conservative upper limit and strong indication that the actual level of cavity length fluctuations is much smaller. The exact level of vibrations at the second stage of the used here cryocooler (PT-420RM by Cryomech) is not known, but based on data for similar solutions [47], we estimate the amplitude of the fluctuations at few microns, which means that in our system the attenuation of mechanical vibration from cryocooler to cavity length is much better than three orders of magnitude. This is the best quantitative analysis we can provide with the presently available to us instrumentation. We do develop a new system of laser locking to ultra-stable reference optical cavity, which will allow us provide in the future much better quantitative analysis of the cavity length fluctuations. A crucial conclusion from the perspective of high-precision cavity-enhanced spectroscopy applications is that we already reached the level of mechanical fluctuations of cavity length much lower than the corresponding laser frequency fluctuation meaning that the mechanical noise attenuation is already sufficient to address many scientific challenges at the frontier of physics and chemistry as shown in Ref. [39].

The larger mechanical noise attenuation can be attributed to the large mass of the cryogenic chamber incorporating the optical cavity, which acts as an effective inertial element suppressing mechanical disturbances, as well as to the use of flexible thermal links between the stages responsible for heat transport. These links reduce the mechanical coupling between the cryocooler and the cavity assembly, thereby limiting the transmission of vibrations while maintaining efficient thermal conduction. Furthermore, the system exhibits significantly reduced sensitivity to external mechanical perturbations compared to room-temperature optical cavities used in our laboratory. In particular, mechanical shocks applied to the optical table, which typically lead to immediate loss of lock in our conventional cavities [48], have only a minor effect on the cryogenic system, demonstrating its enhanced mechanical robustness and effective vibration isolation.

8. Conclusion

In this paper, we demonstrated a cryogenic vacuum chamber that is characterized by high stability and high uniformity of temperature, as well as a low level of mechanical noise and vibrations. It allowed us to extend, for the first time, the optical-cavity-enhanced spectroscopy technologies from room temperatures down to a deep cryogenic regime (to below 5 K). The strict requirements necessary to operate optical resonators are met by equipping the system with multiple stages of heavy copper blocks and flexible thermal connectors that altogether serve as an excellent low-pass filter for temperature fluctuations (mainly originating from cryocooler operation cycle). We also demonstrated that this design isolates the cryogenic vacuum system from external noise and cryocooler vibrations suitably well for optical cavity operation. The system design ensures nearly perfect temperature uniformity (74 μK) across the main copper cylinder of the experimental cryogenic chamber that is critical for ultra-accurate spectroscopic measurements at deep cryogenic conditions. The temperature differences are larger (21 mK) for chamber doors; this does not, however, influence the operation of the optical cavity, which is thermally anchored only to the main copper cylinder. Recently, we demonstrated [39] that this system opens a way to new types of measurements that were not possible before, such as an accurate test of the quantum electrodynamics for molecules, realization of the primary SI standards for temperature, concentration, and pressure in the deep cryogenic regime, measurement of the H_2 phase diagram, and determination of the ortho-para spin isomer conversion rate. This work provides comprehensive technological insights and performance characterization of the system, thereby offering practical guidance for the design and implementation of advanced cryogenic platforms for high-precision measurements across diverse scientific and technological applications.

CRediT authorship contribution statement

Kamil Leon Sołtys: Writing – review & editing, Writing – original draft, Visualization, Validation, Project administration, Methodology, Investigation, Formal analysis, Data curation, Conceptualization. **Michał Słowiński:** Writing – review & editing, Writing – original draft, Visualization, Validation, Software, Project administration, Methodology, Investigation, Formal analysis, Data curation, Conceptualization. **Marcin Makowski:** Methodology, Investigation, Data curation. **Bogdan Bednarski:** Methodology, Investigation, Data curation, Formal analysis, Investigation, Visualization. **Kamil Stankiewicz:** Methodology, Investigation. **Paweł Olejarczyk:** Visualization, Investigation. **Szymon Wójtewicz:** Methodology, Investigation. **Daniel Lisak:** Writing – review & editing, Writing – original draft, Methodology, Investigation, Funding acquisition. **Mariusz Piwiński:** Project administration, Methodology, Investigation. **Piotr Wcisło:** Writing – review & editing, Writing – original draft, Visualization, Methodology, Investigation, Funding acquisition, Formal analysis, Conceptualization.

Declaration of competing interest

The authors declare that they have no known competing financial interests or personal relationships that could have appeared to influence the work reported in this paper.

Acknowledgements

We thank M. Drewsen and J. Glässel for discussions on cryogenic technologies. This research was funded by the European Union (Grant No 101075678, ERC-2022-STG, H2TRAP). Views and opinions expressed are, however, those of the author(s) only and do not necessarily reflect those of the European Union or the European Research Council Executive Agency. Neither the European Union nor the granting authority can be held responsible for them. This work is a part of the 23FUN04 COMOMET project that has received funding from the European Partnership on Metrology, co-financed from the European Union's Horizon Europe Research and Innovation Programme and by the Participating States. Funder ID 10.13039/100019599. We gratefully acknowledge Polish high-performance computing infrastructure PLGrid (HPC Center: ACK Cyfronet AGH) for providing computer facilities and support within computational grant no. PLG/2026/019877. Created using resources provided by Wroclaw Centre for Networking and Supercomputing (http://wcss.pl). The work was supported by the National Science Centre in Poland through Projects Nos. 2025/58/A/ST2/00116 (M.M., M.P., P.W.), 2022/46/E/ST2/00282 (K.L.S., M.S., P.O.), 2024/55/B/ST2/01038 (D.L.), 2021/42/E/ST2/00152 (B.B., S.W.). K.S. contribution is supported by budgetary funds within the Minister of Education and Science program "Perły Nauki", Project No. PN/01/0196/2022. The research was conducted using infrastructure from National Laboratory of Photonic and Quantum Technologies and is part of the program of the National Laboratory FAMO in Toruń, Poland.

Data availability

The data that support the plots within this paper and other findings of this study are publicly available in the Repository for Open Data (RepOD) [49].

Appendix A

The conductive heat transfer through the thermal links (stainless steel wires and titanium elements) can be estimated using a straightforward approximation

$$Q_c(T_H, T_L) = \frac{A}{L} \times \lambda\left(\frac{T_H + T_L}{2}\right)(T_H - T_L), \tag{A.1}$$

where A and L denote the cross-sectional area and length of the link, respectively, $\lambda(T)$ is the temperature-dependent thermal conductivity, and T_H and T_L are the temperatures at the high- and low-temperature ends of the thermal link. This expression is used here only as a reference to illustrate the accuracy of this commonly employed approximation. In our analysis, the conductive heat loads are instead evaluated using the more accurate full integral expression:

$$Q(T_H, T_L) = \frac{A}{L}\int_{T_L}^{T_H} \lambda(T)\mathrm{d}T. \tag{A.2}$$

Both Eqs. (A.1) and (A.2) yield very similar results overall. The use of the approximate approach introduces only sub-percent discrepancies within the linear regime (see Fig. 12), where the area under the dashed (approximate) and solid (exact) curves is visually indistinguishable. However, in the low-temperature region, the exact expression may be preferable, as deviations in the non-linear regime can reach up to approximately 10%.

The thermal conductivity of titanium depends on material composition and variations can lead to differences in estimated heat loads of up to a factor of three [41]. In this work, all titanium elements are made of Grade 5 titanium (Ti-6Al-4V) [51–53], and the corresponding temperature-dependent thermal conductivities are shown in Fig. 12.

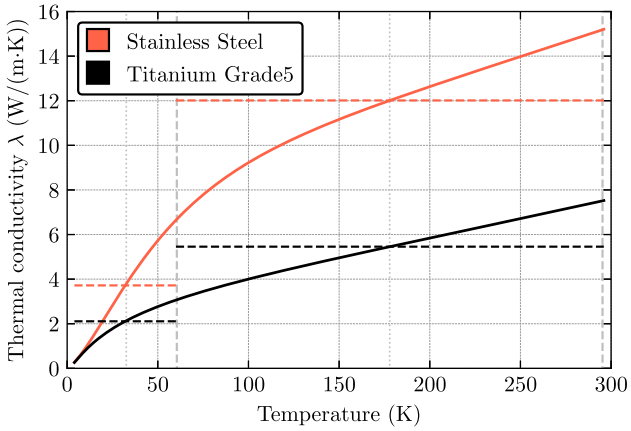

Fig. 12. Thermal conductivity functions for stainless steel (red) [50] and titanium Grade 5 (black) [51–53]. The dashed lines show the crude approximation values based on the mean temperature of the thermal link (see: Eq. (A.1)). The grey dashed and dotted lines indicate the lower and upper bounds, as well as the midpoints, of the corresponding thermal link configurations.

The results presented in Sections 4 and 5 correspond to three types of thermal links in the system. As a first case, we consider the stainless-steel suspensions between room temperature and the 60 K shield (see the green lines in Fig. 1), which yield heat loads of 41.9 mW per wire for the rod-shield suspension and 87.9 mW per wire for the chamber suspension. This corresponds to a total heat load of 519 mW from all stainless-steel wires. Using the approximation given by Eq. (A.1), these values are overestimated by approximately 2.5%, giving a total of 532 mW.

The second category consists of the titanium wire suspensions between the 60 K shield and 4 K stage (see the blue lines in Fig. 1). Due to the geometry of these elements, all links exhibit the same heat load of 2.55 mW per rod, resulting in a total conductive heat load of 20.4 mW for the full set. Using the approximation given by Eq. (A.1), the corresponding total is overestimated by approximately 7%, giving 21.8 mW.

The third category consists of the titanium support rods of the 60 K shield. Each rod contributes a heat load of 173.6 mW, resulting in a total conductive heat load of 694.2 mW for the full set. Using the approximation given by Eq. (A.1), the corresponding total is overestimated by approximately 0.75%, giving 699.4 mW.

Appendix B

To quantify the thermal-expansion mismatch discussed in Section 5.4, we consider the corresponding joint in our setup consisting of a copper rod, thermal straps, and stainless-steel fastening elements, as shown in Fig. 9. For a 58.41 mm copper component with two 4 mm-thick thermal straps (all dimensions at 296 K), the total contraction upon cooling to operating temperature is 186.9 µm, compared to 176.2 µm for the stainless-steel fastening elements. This results in a differential displacement of 10.69 µm, which, if uncompensated, would significantly reduce the initial clamping force by 320 N.

Introducing Invar spacers between the copper and stainless-steel components effectively suppresses this mismatch due to the much smaller thermal expansion coefficient of Invar [54]. Even though the

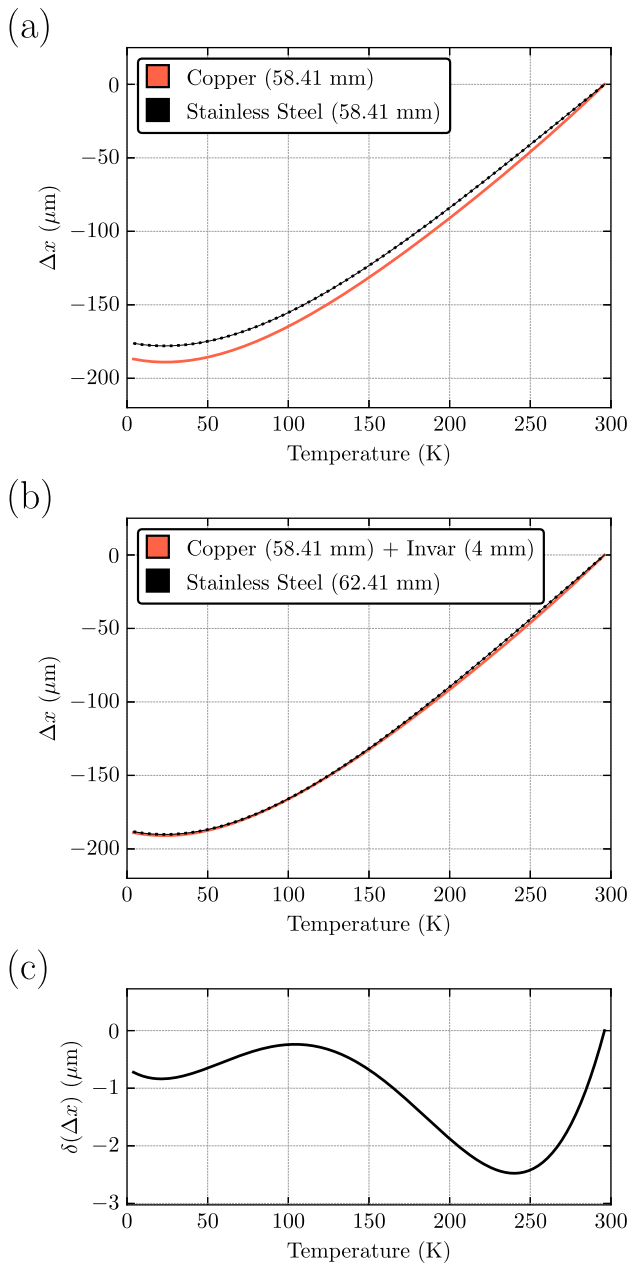

Fig. 13. Comparison of material shrinkage behaviour across different thermal link configurations. (a) Shrinkage without Invar: copper (red) and stainless steel (black) are shown. (b) Shrinkage with Invar added, where the red curve represents the copper–Invar composite, compared to stainless steel (black). (c) Difference between the curves shown in panel (b), highlighting the effect of adding Invar on the relative thermal contraction behaviour. In panels (a) and (b), the sizes indicated in the legend correspond to the element dimensions at room temperature.

Invar plates are only thin (with total thickness of 4 mm), they are sufficient to compensate for different contraction, reducing the differential displacement down to 0.72 μm, as illustrated in Fig. 13. This obscures the initial reduction in clamping force, limiting it to approximately 20 N.

References

[1] H. Wu, N. Stolarczyk, Q.-H. Liu, C.-F. Cheng, T.-P. Hua, Y.R. Sun, S.-M. Hu, Opt. Express 27 (2019) 37559.
[2] E. Wiens, C.J. Kwong, T. Müller, S. Schiller, Rev. Sci. Instrum. 91 (2020) 045112.
[3] E. Wiens, S. Schiller, Rev. Sci. Instrum. 92 (2021) 095101.
[4] Y. Ye, L. He, Y. Sun, F. Zhang, Z. Wang, Y. Zheng, Z. Lu, Sensors 21 (2021) 4696.
[5] Q.-H. Liu, Y.-N. Lv, C.-L. Zou, C.-F. Cheng, S.-M. Hu, Phys. Rev. A 106 (2022) 062805.
[6] W.-W. Wang, Z.-A. Chen, H. Zhang, S. Du, R. Wu, C. Qiao, S. Kuang, X. Zhang, Front. Phys. 11 (2023) 1176783.
[7] F.M.J. Cozijn, M.L. Diouf, W. Ubachs, Phys. Rev. Lett. 131 (2023) 073001.
[8] W. Ubachs, F.M.J. Cozijn, M.L. Diouf, C. Lauzin, H. Jóźwiak, P. Wcisło, Phys. Rev. Lett. 135 (2025) 223201.
[9] Q.-H. Liu, Y.-N. Lv, C.-F. Cheng, S.-M. Hu, Mol. Phys. (2026) e2641679.
[10] P.B. Antohi, D. Schuster, G.M. Akselrod, J. Labaziewicz, Y. Ge, Z. Lin, W.S. Bakr, I.L. Chuang, Rev. Sci. Instrum. 80 (2009) 013103.
[11] M. Schwarz, O.O. Versolato, A. Windberger, F.R. Brunner, T. Ballance, S.N. Eberle, J. Ullrich, P.O. Schmidt, A.K. Hansen, A.D. Gingell, M. Drewsen, J.R. Crespo López-Urrutia, Rev. Sci. Instrum. 83 (2012) 083115.
[12] P. Micke, J. Stark, S.A. King, T. Leopold, T. Pfeifer, L. Schmöger, M. Schwarz, L.J. Spieß, P.O. Schmidt, J.R. Crespo López-Urrutia, Rev. Sci. Instrum. 90 (2019) 065104.
[13] C. Miossec, M. Hejduk, R. Pandey, N.J.A. Coughlan, B.R. Heazlewood, Rev. Sci. Instrum. 93 (2022) 033201.
[14] J.M. Cornejo, J. Brombacher, J.A. Coenders, M. von Boehn, T. Meiners, M. Niemann, S. Ulmer, C. Ospelkaus, Phys. Rev. Res. 6 (2024) 033233.
[15] E. Oelker, R.B. Hutson, C.J. Kennedy, L. Sonderhouse, T. Bothwell, A. Goban, D. Kedar, C. Sanner, J.M. Robinson, G.E. Marti, D.G. Matei, T. Legero, M. Giunta, R. Holzwarth, F. Riehle, U. Sterr, J. Ye, Nat. Photonics 13 (2019) 714.
[16] A. Aeppli, K. Kim, W. Warfield, M.S. Safronova, J. Ye, Phys. Rev. Lett. 133 (2024) 023401.
[17] G. Pagano, P.W. Hess, H.B. Kaplan, W.L. Tan, P. Richerme, P. Becker, A. Kyprianidis, J. Zhang, E. Birckelbaw, M.R. Hernandez, Y. Wu, C. Monroe, Quantum Sci. Technol. 4 (2018) 014004.
[18] N.R. Hutzler, H.-I. Lu, J.M. Doyle, Chem. Rev. 112 (2012) 4803.
[19] S. Truppe, M. Hambach, S.M. Skoff, N.E. Bulleid, J.S. Bumby, R.J. Hendricks, E.A. Hinds, B.E. Sauer, M.R. Tarbutt, J. Modern Opt. 65 (2017) 648.
[20] P.B. Changala, M.L. Weichman, K.F. Lee, M.E. Fermann, J. Ye, Science 363 (2019) 49.
[21] A.R.W. McKellar, J. Chem. Phys. 92 (1990) 3261.
[22] L.N. Fletcher, M. Gustafsson, G.S. Orton, Astrophys. J. Suppl. Ser. 235 (2018) 24.
[23] S. Bauerecker, E. Dartois, Icarus 199 (2009) 564.
[24] S. Kassi, C. Lauzin, J. Chaillot, A. Campargue, Phys. Chem. Chem. Phys. 24 (2022) 23164.
[25] L. Gianfrani, S.-M. Hu, W. Ubachs, Riv. Nuovo Cimento 47 (2024) 229.
[26] T. Dubielzig, S. Halama, H. Hahn, G. Zarantonello, M. Niemann, A. Bautista-Salvador, C. Ospelkaus, Rev. Sci. Instrum. 92 (2021) 043201.
[27] D.M. Hartsell, J.M. Gray, C.M. Shappert, N.L. Gostin, R.A. McGill, H.N. Tinkey, C.R. Clark, K.R. Brown, Appl. Phys. Lett. 128 (2026) 034001.
[28] B. Deng, S. Yang, X. Xie, Y. Wang, X. Bian, L. Gong, Q. Li, Cryogenics 100 (2019) 114.
[29] A.R. Hashmi, H. Wang, R. Ji, B. Wang, A.A. Rahman, F. Saadat, Y. Gao, Z. Gan, Int. J. Refrig. 175 (2025) 196.
[30] S. Jacob, S. Kasthurirengan, R. Karunanithi, Cryogenics 32 (1992) 1137.
[31] H. Neumann, Cryogenics 44 (2004) 93.
[32] J.E. Fesmire, W.L. Johnson, Cryogenics 89 (2018) 58.
[33] T. Tomaru, T. Suzuki, T. Haruyama, T. Shintomi, A. Yamamoto, T. Koyama, R. Li, Cryogenics 44 (2004) 309.
[34] A. Chijioke, J. Lawall, Cryogenics 50 (2010) 266.
[35] C. Wang, J.G. Hartnett, Cryogenics 50 (2010) 336.
[36] W. Zhang, J.M. Robinson, L. Sonderhouse, E. Oelker, C. Benko, J.L. Hall, T. Legero, D.G. Matei, F. Riehle, U. Sterr, J. Ye, Phys. Rev. Lett. 119 (2017) 243601.
[37] C. Pan, J. Hu, H. Zhang, Y. Song, D. Han, W. Liu, H. Chen, M. Plimmer, F. Sparasci, E. Luo, B. Gao, L. Pitre, Cryogenics 109 (2020) 103096.
[38] G. Pizzo, V. Dall'Oglio, J. Low Temp. Phys. 210 (2022) 506.
[39] K. Stankiewicz, M. Makowski, M. Słowiński, K.L. Sołtys, B. Bednarski, H.J. Jóźwiak, N. Stolarczyk, M. Narożnik, D. Kierski, S. Wójtewicz, A. Cygan, G. Kowzan, P. Masłowski, M. Piwiński, D. Lisak, P. Wcisło, Nat. Phys. 22 (2026) 637.
[40] N. Derimow, J.T. Benzing, T.S. Weeks, Cryogenics 149 (2025) 104105.
[41] J. Ekin, Experimental Techniques for Low-Temperature Measurements: Cryostat Design, Material Properties and Superconductor Critical-Current Testing, Oxford University Press, Oxford, 2006.
[42] W. Zhao, W. Su, L. Li, D. Fang, N. Chen, Met. Mater. Int. 27 (2020) 3214–3224.
[43] L.J. Salerno, P. Kittel, A.L. Spivak, Cryogenics 34 (1994) 649.
[44] Technical Reference Center, Cryogenic material properties: Ofhc copper (uns c10100/c10200), 2010, (Accessed 22 June 2026).
[45] Technical Reference Center, Cryogenic material properties: 304 stainless (uns s30400), 2010, (Accessed 22 June 2026).
[46] M. Słowiński, M. Makowski, K.L. Sołtys, K. Stankiewicz, S. Wójtewicz, D. Lisak, M. Piwiński, P. Wcisło, Rev. Sci. Instrum. 93 (2022) 115003.
[47] C. Wang, P.E. Gifford, AIP Conf. Proc. 613 (2002) 641.
[48] D. Lisak, V. D'Agostino, S. Wójtewicz, A. Cygan, M. Gibas, P. Wcisło, R. Ciuryło, K. Bielska, Phys. Rev. Lett. 135 (2025) 103201.

[49] Kamil Leon Sołtys, Michał Słowiński, Marcin Makowski, Bogdan Bednarski, Kamil Stankiewicz, Paweł Olejarczyk, Szymon Wójtewicz, Daniel Lisak, Mariusz Piwiński, Piotr Wcisło, Data for manuscript entitled "a novel experimental platform for new types of optical measurements in the deep cryogenic regime", 2026, http://dx.doi.org/10.18150/2FBBBS.
[50] R.S. Graves, T.G. Kollie, D.L. McElroy, K.E. Gilchrist, Int. J. Thermophys. 12 (1991) 409.
[51] W.T. Ziegler, J.C. Mullins, S.C.P. Hwa, Adv. Cryog. Eng. 8 (1963) 268.
[52] O. Umezawa, K. Ishikawa, Cryogenics 32 (1992) 873.
[53] L. Risegari, M. Barucci, L. Lolli, G. Ventura, J. Low Temp. Phys. 151 (2008) 645.
[54] D. Mann, LNG Materials and Fluids, first ed., National Bureau of Standards, Cryogenics Division, 1977.